Journal of Science and Transport Technology
Journal homepage: https://jstt.vn/index.php/en

Semi-analytical approach for nonlinear dynamic responses of complex curved functionally graded graphene metal matrix reinforced panels subjected to impulse loads

Nguyen Thi Phuong[1,2], Kieu Lan Huong[3*], Truong Thi Hue[4]
[1]Mechanics of Advanced Materials and Structures, Institute for Advanced Study in Technology, Ton Duc Thang University, Ho Chi Minh City, Vietnam
[2]Faculty of Civil Engineering, Ton Duc Thang University, Ho Chi Minh City, Vietnam
[3]Graduate University of Science and Technology, Vietnam Academy of Science and Technology, Hanoi, Vietnam
[4]Mechanics of Advanced Materials and Structures, University of Transport Technology, Hanoi, Vietnam

Article info
Type of article:
Original research paper

DOI:
https://doi.org/10.58845/jstt.utt.2026.en.6.2.150-170

***Corresponding author:**
Email address:
huongkl@utt.edu.vn

Received: 09/10/2025
Received in Revised Form: 12/11/2025
Accepted: 16/12/2025

Abstract: This study develops a semi-analytical framework to investigate the nonlinear dynamic behavior of functionally graded graphene-reinforced metal matrix composite (FG-GRMMC) shallow panels with complex curvatures under thermal environments. Three panel geometries, cylindrical, parabolic, and sinusoid, are examined under impulsive loading conditions, including finite duration step and triangular blast loads. The analysis is formulated within the higher-order shear deformation theory (HSDT), incorporating von Kármán geometric nonlinearities. To address the geometric complexity, the stress function is approximated using an average-based like-Galerkin technique that satisfies the compatibility condition. The nonlinear governing equations of motion are derived via the Lagrange principle, with structural damping modeled through the Rayleigh dissipation function. Numerical simulations employing the fourth-order Runge-Kutta method are conducted to capture the time-dependent deflection responses. The results provide insights into the influence of panel geometry, graphene distribution, and impulse load characteristics on the nonlinear dynamic performance of FG-GRMMC panels.

Keywords: Functionally graded graphene metal matrix reinforced composite, Impulse load, Dynamic response, Higher-order shear deformation theory, Thermal environment, Complex curved panel.

1. Introduction

Functionally graded composite materials (FGMs) have emerged as a prominent class of advanced structural materials due to their ability to tailor mechanical and thermal properties continuously across the thickness. This gradation enhances structural performance under complex service conditions, making FGMs highly suitable for applications in aerospace, civil infrastructure, shipbuilding, and other engineering domains. As a result, the mechanical behavior of FGM structures has attracted considerable attention in recent

decades. Numerous studies have focused on their stability and nonlinear response, including investigations into buckling phenomena [1, 2], mechanical postbuckling behavior [3], and thermal-induced instability [4–7]. Furthermore, the nonlinear postbuckling analysis of FGM plates reinforced by orthogonal and oblique stiffeners has been explored using advanced techniques such as the improved smeared stiffener method [5–7].

Research on structures reinforced with carbon nanotubes (CNTs) has also proliferated, given their exceptional mechanical and thermal properties at the nanoscale. Functionally graded carbon nanotube-reinforced composites (FG-CNTRCs) have been the subject of extensive investigation across a range of structural behaviors. Zhang et al. [8–10], employing the element-free Ritz method in conjunction with first-order shear deformation theory (FSDT), analyzed the vibration, nonlinear bending, and buckling responses of FG-CNTRC plates. Building on this, Zhang and Liew [11–13] examined large geometrically nonlinear deformations in quadrilateral and skew CNT-reinforced plates. Yang et al. [14] adopted higher-order shear deformation theory (HSDT) with von Kármán kinematic nonlinearity to explore the large-amplitude vibrations of FG-CNTRC laminates with negative Poisson's ratios under uniform thermal fields. In parallel, the Differential Quadrature Method (DQM), originally proposed by Bellman et al. [15], has gained traction as a powerful numerical tool for solving complex structural problems. Alibeigloo and Emtehani [16] applied DQM to study free vibration and bending of FG-CNTRC plates under various boundary constraints, while Jiao et al. [17] investigated buckling under partially distributed edge compression. The Ritz method has also been effectively utilized by Kiani and co-authors [18–20] to evaluate shear buckling and dynamic responses of FG-CNTRC panels with different geometries. More recently, Foroutan et al. [21, 22] conducted comprehensive studies on the nonlinear vibration and hydrothermal buckling of imperfect FG-CNTRC cylindrical panels under pressure loads and thermal gradients.

In recent years, graphene has emerged as a highly effective reinforcement material due to its superior thermomechanical properties, comparable to or surpassing those of carbon nanotubes. When embedded in polymer matrices, graphene sheets can significantly enhance the stiffness, strength, and thermal stability of composite structures. This has led to the development of functionally graded graphene-reinforced composites (FG-GRCs), in which the volume fraction of graphene is varied through the thickness to optimize performance under mechanical and thermal loads. Several studies have explored the nonlinear behaviors of FG-GRC laminates and shells. Using perturbation techniques, researchers have analyzed mechanical and thermal buckling, postbuckling, vibration, and dynamic instability phenomena in FG-GRC plates and cylindrical panels [23–27]. Additionally, the NURBS-based isogeometric approach has been applied to investigate the thermal postbuckling and vibration responses of FG-GRC laminates with temperature-dependent properties [28, 29]. Beyond flat and cylindrical configurations, complex shell geometries such as conical shells, toroidal segments, and other curved structures have also been examined within the FG-GRC framework [30–35].

While most previous studies have concentrated on graphene-reinforced composites with polymer matrices, recent advancements in nanocomposite technology have paved the way for the development of metal matrix composites reinforced with graphene. Among these, functionally graded graphene-reinforced metal matrix composite (FG-GRMMC) offers enhanced thermal conductivity, higher strength-to-weight ratios, and improved resistance to harsh environments compared to their polymer-based counterparts [36]. These characteristics make FG-

GRMMCs particularly suitable for structural applications subjected to severe thermal and dynamic loads. Some previous works focused on the nonlinear buckling, postbuckling and vibration problems of plates and cylindrical panels [37-38] using the HSDT and perturbation technique.

Despite the extensive research on FGM, FG-CNTRC, FG-GRC, FG-GRMMC panels most existing studies have focused on structural responses under static or harmonic loading conditions. In contrast, the dynamic behavior of FG-GRMMC panels, particularly complex curved panels under impulsive loading, remains relatively underexplored.

In this context, the present work proposes a new semi-analytical approach to investigate the nonlinear dynamic responses of FG-GRMMC shallow panels with cylindrical, parabolic, and sinusoid geometries. The formulation is based on the HSDT including von Kármán-type geometric nonlinearities. An approximate stress function is employed to satisfy the compatibility condition in an average sense, while the governing equations are derived via the Lagrange principle and include damping effects through the Rayleigh dissipation function. Two types of impulsive loads, including finite duration step and triangular blast loads, are applied, and numerical simulations are performed using the Runge-Kutta method to evaluate time-dependent deflection responses. The study aims to provide insight into the influence of geometric configuration, graphene distribution, and loading characteristics on the nonlinear dynamic behavior of FG-GRMMC panels.

2. Configuration and material designs

Graphene is distributed in copper matrix with four volume fractions as 0.05, 0.07, 0.09, 0.11, and 0.13 and is designed piecewisely through ten layers in the thickness direction of the panel. As can be seen in Fig. 1, the functionally graded laws of graphene can be considered in four cases as FG-V with volume fractions of layers $[(0.13)_2/(0.11)_2/(0.09)_2/(0.07)_2/(0.05)_2]$, FG-A with volume fractions of layers $[(0.05)_2/(0.07)_2/(0.09)_2/(0.11)_2/(0.13)_2]$, FG-X with fractions of layers $[(0.13)/(0.11)/(0.09)/(0.07)/(0.05)]_S$, and FG-O with fractions of layers $[(0.05)/(0.07)/(0.09)/(0.11)/(0.13)]_S$, meanwhile, for reference value, the uniformly distributed (UD) law with volume fractions of layers $[0.09]_{10}$ is considered. For simplicity, the distribution laws of the panel are called according to the distribution laws of the shell skin. The graphene direction of GRMMC layers can be different and arranged through shell thickness as $(0)_{10}$, $(0/90)_{5T}$, and $(0/90/0/90/0)_S$. In this paper, thermo-elastic constants of GRMMC are referred from the report of Fan et al. [36].

The shallow FG-GRMMC panels are considered with three configurations, including cylindrical, sinusoid, and parabolic forms, and are placed in the quasi-Cartesian coordinate system, as shown in Fig. 1. The geometrical parameters of panels are denoted with the total thickness h, the rise of central point H, longitudinal edge a, and circumferential edge b.

The configuration function of the curved surface of the parabolic and sinusoid panels in the circumferential direction can be considered respectively as follows

$$z_{(p)} = -H\left(\frac{4y^2}{b^2} - \frac{4y}{b}\right), \qquad z_{(s)} = H\sin\left(\frac{\pi y}{b}\right). \tag{1}$$

The radius of curvature can be achieved from Eq. (1), respectively, for the parabolic and sinusoid panels, as

$$R_{(s)} = \frac{\left[H_y^2\pi^2\cos^2\left(\frac{\pi y}{b}\right) + b^2\right]^{1.5}}{bH_y\pi^2\sin\left(\frac{\pi y}{b}\right)}, \qquad R_{(p)} = \frac{\left[b^4 + 16H_y^2(b-2y)^2\right]^{1.5}}{8b^4H_y}. \tag{2}$$

The stress-strain relationships of Hookian law in conjunction with the uniform temperature change for the panels are written by

$$\begin{bmatrix}\sigma_x\\ \sigma_y\\ \sigma_{xy}\end{bmatrix}=\begin{bmatrix}\hat{Q}_{11}^{*} & \hat{Q}_{12}^{*} & 0\\ \hat{Q}_{12}^{*} & \hat{Q}_{22}^{*} & 0\\ 0 & 0 & \hat{Q}_{66}^{*}\end{bmatrix}\begin{bmatrix}\varepsilon_x-\alpha_{11}\Delta T\\ \varepsilon_y-\alpha_{22}\Delta T\\ \gamma_{xy}\end{bmatrix},\quad (3)$$

$$\sigma_{xz}=\hat{Q}_{44}^{*}\gamma_{xz},\quad \sigma_{yz}=\hat{Q}_{55}^{*}\gamma_{yz},$$

where ΔT is the uniform temperature rise from the free thermal stress state to the deformed state of panel. The reduced stiffnesses can be made out as

$$\hat{Q}_{11}^{*}=\frac{E_{11}}{1-\nu_{12}\nu_{21}},$$

$$\hat{Q}_{12}^{*}=\frac{\nu_{21}E_{11}}{1-\nu_{12}\nu_{21}},$$

$$\hat{Q}_{22}^{*}=\frac{E_{22}}{1-\nu_{12}\nu_{21}},$$

$$\hat{Q}_{66}^{*}=G_{12},\quad \hat{Q}_{44}^{*}=\hat{Q}_{55}^{*}=0.5G_{12}.$$

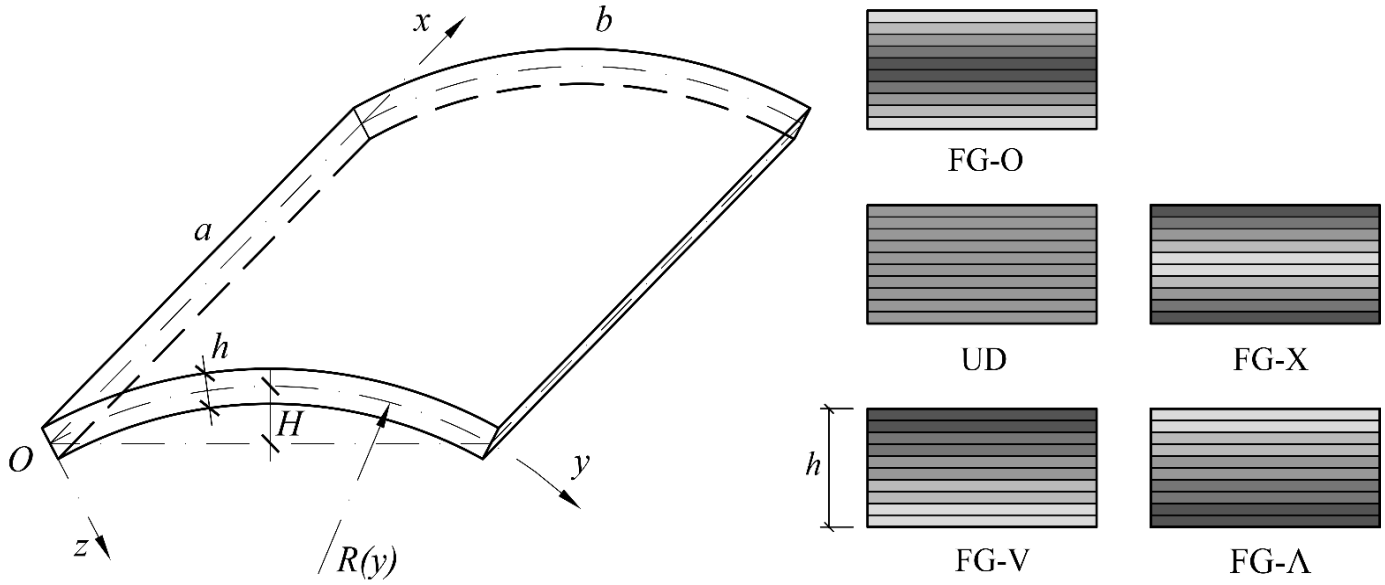

Fig. 1. Complex curved FG-GRMMC panels and material distributions

3. Basic Formulations

The panel in this paper are considered with the large deflection assumption. The governing formulas are established using the HSDT with nonlinear large deflection terms and imperfect deflection $\bar{w}$. The relations between strains $\varepsilon_x,\varepsilon_y,\gamma_{xy},\gamma_{xz},\gamma_{yz}$ and displacements u,v,w and rotations ϕ_x,ϕ_y can be formulated

$$\begin{Bmatrix}\varepsilon_x\\ \varepsilon_y\\ \gamma_{xy}\end{Bmatrix}=\begin{Bmatrix}\hat{\varepsilon}_x^{[0]}\\ \hat{\varepsilon}_y^{[0]}\\ \hat{\gamma}_{xy}^{[0]}\end{Bmatrix}+z\begin{Bmatrix}\hat{\chi}_x^{[1]}\\ \hat{\chi}_y^{[1]}\\ \hat{\chi}_{xy}^{[1]}\end{Bmatrix}+z^3\begin{Bmatrix}\hat{\chi}_x^{[3]}\\ \hat{\chi}_y^{[3]}\\ \hat{\chi}_{xy}^{[3]}\end{Bmatrix},\quad (4)$$

$$\begin{Bmatrix}\gamma_{xz}\\ \gamma_{yz}\end{Bmatrix}=\begin{Bmatrix}\hat{\gamma}_{xz}^{[0]}\\ \hat{\gamma}_{yz}^{[0]}\end{Bmatrix}+z^2\begin{Bmatrix}\hat{\chi}_{xz}^{[2]}\\ \hat{\chi}_{yz}^{[2]}\end{Bmatrix},$$

where

$$\begin{Bmatrix}\hat{\varepsilon}_x^{[0]}\\ \hat{\varepsilon}_y^{[0]}\\ \hat{\gamma}_{xy}^{[0]}\end{Bmatrix}=\begin{Bmatrix}u_{,x}+w_{,x}^2/2+w_{,x}\bar{w}_{,x}\\ v_{,y}+w_{,y}^2/2+w_{,y}\bar{w}_{,y}-w/R(y)\\ v_{,x}+u_{,y}+w_{,x}w_{,y}+w_{,y}\bar{w}_{,x}+w_{,x}\bar{w}_{,y}\end{Bmatrix}$$

$$\begin{Bmatrix}\hat{\chi}_x^{[1]}\\ \hat{\chi}_y^{[1]}\\ \hat{\chi}_{xy}^{[1]}\end{Bmatrix}=\begin{Bmatrix}\phi_{x,x}\\ \phi_{y,y}\\ \phi_{y,x}+\phi_{x,y}\end{Bmatrix},$$

$$\begin{Bmatrix}\hat{\chi}_x^{[3]}\\ \hat{\chi}_y^{[3]}\\ \hat{\chi}_{xy}^{[3]}\end{Bmatrix}=-\frac{4}{3h^2}\begin{Bmatrix}w_{,xx}+\phi_{x,x}\\ w_{,yy}+\phi_{y,y}\\ \phi_{y,x}+2w_{,xy}+\phi_{x,y}\end{Bmatrix},$$

$$\begin{Bmatrix}\hat{\gamma}_{xz}^{[0]}\\ \hat{\gamma}_{yz}^{[0]}\end{Bmatrix}=\begin{Bmatrix}w_{,x}+\phi_x\\ w_{,y}+\phi_y\end{Bmatrix},\quad (5)$$

$$\begin{Bmatrix}\hat{\chi}_{xz}^{[2]}\\ \hat{\chi}_{yz}^{[2]}\end{Bmatrix}=-\frac{4}{h^2}\begin{Bmatrix}w_{,x}+\phi_x\\ w_{,y}+\phi_y\end{Bmatrix}.$$

The relationships between internal forces and moments with the strains, rotations, and deflection for the three forms of FG-GRMMC panels are derived as follows:

$$\begin{aligned}
N_x &= e_{11}\hat{\varepsilon}_x^{[0]} + e_{12}\hat{\varepsilon}_y^{[0]} + d_{11}\hat{\chi}_x^{[1]} + d_{12}\hat{\chi}_y^{[1]} + a_{11}\hat{\chi}_x^{[3]} \\
&\quad + a_{12}\hat{\chi}_y^{[3]} - \Phi_{1x}^{*}\Delta T, \\
N_y &= e_{12}\hat{\varepsilon}_x^{[0]} + e_{22}\hat{\varepsilon}_y^{[0]} + d_{12}\hat{\chi}_x^{[1]} + d_{22}\hat{\chi}_y^{[1]} + a_{12}\hat{\chi}_x^{[3]} \\
&\quad + a_{22}\hat{\chi}_y^{[3]} - \Phi_{1y}^{*}\Delta T, \\
N_{xy} &= e_{66}\hat{\gamma}_{xy}^{[0]} + d_{66}\hat{\chi}_{xy}^{[1]} + a_{66}\hat{\chi}_{xy}^{[3]},
\end{aligned} \tag{6a}$$

$$\begin{aligned}
M_x &= d_{11}\hat{\varepsilon}_x^{[0]} + d_{12}\hat{\varepsilon}_y^{[0]} + b_{11}\hat{\chi}_x^{[1]} + b_{12}\hat{\chi}_y^{[1]} + c_{11}\hat{\chi}_x^{[3]} \\
&\quad + c_{12}\hat{\chi}_y^{[3]} - \Phi_{2x}^{*}\Delta T, \\
M_y &= d_{12}\hat{\varepsilon}_x^{[0]} + d_{22}\hat{\varepsilon}_y^{[0]} + b_{12}\hat{\chi}_x^{[1]} + b_{22}\hat{\chi}_y^{[1]} + c_{12}\hat{\chi}_x^{[3]} \\
&\quad + c_{22}\hat{\chi}_y^{[3]} - \Phi_{2y}^{*}\Delta T, \\
M_{xy} &= d_{66}\hat{\gamma}_{xy}^{[0]} + b_{66}\hat{\chi}_{xy}^{[1]} + c_{66}\hat{\chi}_{xy}^{[3]},
\end{aligned} \tag{6b}$$

$$\begin{aligned}
T_x &= a_{11}\hat{\varepsilon}_x^{[0]} + a_{12}\hat{\varepsilon}_y^{[0]} + c_{11}\hat{\chi}_x^{[1]} + c_{12}\hat{\chi}_y^{[1]} + h_{11}\hat{\chi}_x^{[3]} \\
&\quad + h_{12}\hat{\chi}_y^{[3]} - \Phi_{4x}^{*}\Delta T, \\
T_y &= a_{12}\hat{\varepsilon}_x^{[0]} + a_{22}\hat{\varepsilon}_y^{[0]} + c_{12}\hat{\chi}_x^{[1]} + c_{22}\hat{\chi}_y^{[1]} + h_{12}\hat{\chi}_x^{[3]} \\
&\quad + h_{22}\hat{\chi}_y^{[3]} - \Phi_{4y}^{*}\Delta T, \\
T_{xy} &= a_{66}\hat{\gamma}_{xy}^{[0]} + c_{66}\hat{\chi}_{xy}^{[1]} + h_{66}\hat{\chi}_{xy}^{[3]}.
\end{aligned} \tag{6c}$$

The shear forces and the higher-order shear forces Q_x, Q_y and S_x, S_y are presented as

$$\begin{aligned}
Q_x &= f_{44}\hat{\gamma}_{xz}^{[0]} + g_{44}\hat{\chi}_{xz}^{[2]}, Q_y = f_{55}\hat{\gamma}_{yz}^{[0]} + g_{55}\hat{\chi}_{yz}^{[2]}, \\
S_x &= g_{44}\hat{\gamma}_{xz}^{[0]} + l_{44}\hat{\chi}_{xz}^{[2]}, S_y = g_{55}\hat{\gamma}_{yz}^{[0]} + l_{55}\hat{\chi}_{yz}^{[2]}.
\end{aligned} \tag{7}$$

The stiffnesses and thermal forces in Eqs. (6) and (7) can be displayed as

$$\left(e_{ij}, d_{ij}, b_{ij}, a_{ij}, c_{ij}, h_{ij}\right) = \int_{-h/2}^{h/2} \hat{Q}_{ij}^{*}\left(1,\ z, z^2, z^3, z^4, z^6\right) dz, \quad (i, j = 1,2,6),$$

$$\left(f_{ij}, g_{ij}, l_{ij}\right) = \int_{-h/2}^{h/2} \hat{Q}_{ij}^{*}\left(1, z^2, z^4\right) dz, \quad (i, j = 4,5),$$

$$\left(\Phi_{1x}, \Phi_{2x}, \Phi_{4x}\right) = \int_{-h/2}^{h/2} \left(\alpha_{11}\hat{Q}_{11}^{*} + \alpha_{22}\hat{Q}_{12}^{*}\right)\left(1, z, z^3\right) dz,$$

$$\left(\Phi_{1y}, \Phi_{2y}, \Phi_{4y}\right) = \int_{-h/2}^{h/2} \left(\alpha_{11}\hat{Q}_{12}^{*} + \alpha_{22}\hat{Q}_{22}^{*}\right)\left(1, z, z^3\right) dz.$$

Establishing the deformation compatibility equation based on the Eq. (5), presented as

$$\begin{aligned}
&\hat{\varepsilon}_{x,yy}^{[0]} + \hat{\varepsilon}_{y,xx}^{[0]} - \hat{\gamma}_{xy,xy}^{[0]} = -\frac{w_{,xx}}{R(y)} - \bar{w}_{,xx}w_{,yy} \\
&+ w_{,xy}^2 + 2w_{,xy}\bar{w}_{,xy} - w_{,xx}\bar{w}_{,yy} - w_{,xx}w_{,yy}.
\end{aligned} \tag{8}$$

The stress function $\varphi(x, y)$ can be introduced to satisfy as

$$N_x = \varphi_{,yy}, \quad N_{xy} = -\varphi_{,xy}, \quad N_y = \varphi_{,xx}. \tag{9}$$

Combining the expressions of forces and moments (6) and the condition (9), the deformation compatibility equation (8) is re-expressed as

$$\begin{aligned}
&e_{22}^{*}\varphi_{,xxxx} + \left(e_{66}^{*} + 2e_{12}^{*}\right)\varphi_{,xxyy} + e_{11}^{*}\varphi_{,yyyy} + \left(d_{21}^{*} - \frac{4}{3h^2}a_{21}^{*}\right)\phi_{x,xxx} + \left(\frac{4}{3h^2}a_{66}^{*} - \frac{4}{3h^2}a_{11}^{*} + d_{11}^{*} - d_{66}^{*}\right)\phi_{x,xyy} \\
&+ \left(\frac{4}{3h^2}a_{66}^{*} - \frac{4}{3h^2}a_{22}^{*} + d_{22}^{*} - d_{66}^{*}\right)\phi_{y,xxy} + \left(d_{12}^{*} - \frac{4}{3h^2}a_{12}^{*}\right)\phi_{y,yyy} - \frac{4}{3h^2}a_{21}^{*}w_{,xxxx} - \frac{4}{3h^2}\left(a_{11}^{*} + a_{22}^{*} - 2a_{66}^{*}\right)w_{,xxyy} \\
&- \frac{4}{3h^2}a_{12}^{*}w_{,yyyy} + \frac{w_{,xx}}{R(y)} + w_{,xx}\bar{w}_{,yy} + \bar{w}_{,xx}w_{,yy} - w_{,xy}^2 + w_{,xx}w_{,yy} - 2w_{,xy}\bar{w}_{,xy} = 0,
\end{aligned} \tag{10}$$

where

$$e_{11}^{*} = \frac{e_{22}}{e_{11}e_{22} - e_{12}^2}, \ e_{12}^{*} = -\frac{e_{12}}{e_{11}e_{22} - e_{12}^2},$$

$$e_{22}^{*} = \frac{e_{11}}{e_{11}e_{22} - e_{12}^2}, \ e_{66}^{*} = \frac{1}{e_{66}},$$

$$d_{11}^{*} = e_{11}^{*}d_{11} + e_{12}^{*}d_{12}, d_{12}^{*} = e_{11}^{*}d_{12} + e_{12}^{*}d_{22},$$

$$d_{21}^{*} = e_{22}^{*}d_{12} + e_{12}^{*}d_{11}, d_{22}^{*} = e_{22}^{*}d_{22} + e_{12}^{*}d_{12},$$

$$d_{66}^{*} = e_{66}^{*}d_{66}, \ a_{11}^{*} = e_{11}^{*}a_{11} + e_{12}^{*}a_{12},$$

$$a_{12}^{*} = e_{11}^{*}a_{12} + e_{12}^{*}a_{22}, a_{21}^{*} = e_{22}^{*}a_{12} + e_{12}^{*}a_{11},$$

$$a_{22}^{*} = e_{22}^{*}a_{22} + e_{12}^{*}a_{12}, a_{66}^{*} = e_{66}^{*}a_{66}.$$

4. Solving problems

Three mentioned boundary conditions in this study are both simply supported for all four edges, presented as

For the first case, the edges are freely movable (4F), as

$$\begin{aligned} &N_x = N_{0x} = 0,\ T_x = 0,\ M_x = 0,\\ &N_{xy} = 0,\ w = 0,\ \phi_y = 0,\ \text{at } x = 0, a,\\ &N_y = N_{0y} = 0,\ T_y = 0,\ M_y = 0,\\ &N_{xy} = 0,\ w = 0,\ \phi_x = 0,\ \text{at } y = 0, b. \end{aligned} \tag{11}$$

Finally, four immovable and simply supported edges of the panel are considered (4I), as

$$\begin{aligned} &N_x = N_{0x},\ T_x = 0,\ M_x = 0,\ u = 0,\\ &w = 0,\ \phi_y = 0,\ \text{at } x = 0, a,\\ &N_y = N_{0y},\ T_y = 0,\ M_y = 0,\ v = 0,\\ &w = 0,\ \phi_x = 0,\ \text{at } y = 0, b. \end{aligned} \tag{12}$$

To satisfy the three boundary conditions (11, 12), the approximate solutions for the deflection, rotations, and imperfect deflection of three forms of the panel are presented as

$$\begin{aligned} w &= W \sin\left(\frac{m\pi x}{a}\right)\sin\left(\frac{n\pi y}{b}\right),\\ \bar{w} &= \kappa h \sin\left(\frac{m\pi x}{a}\right)\sin\left(\frac{n\pi y}{b}\right),\\ \phi_x &= \Phi_x \cos\left(\frac{m\pi x}{a}\right)\sin\left(\frac{n\pi y}{b}\right),\\ \phi_y &= \Phi_y \sin\left(\frac{m\pi x}{a}\right)\cos\left(\frac{n\pi y}{b}\right), \end{aligned} \tag{13}$$

where the buckling modes of the panel are denoted by m and n; and κ is the imperfect size.

The stress function form can be chosen to be the similar form of the cylindrical panel, taking into account the linear and nonlinear terms, presented as

$$\begin{aligned} \varphi = \varphi_1 \cos\left(\frac{2m\pi x}{a}\right) + \varphi_2 \cos\left(\frac{2n\pi y}{b}\right)\\ + \varphi_3 \sin\left(\frac{m\pi x}{a}\right)\sin\left(\frac{n\pi y}{b}\right)\\ + \frac{1}{2}N_{0y}x^2 + \frac{1}{2}N_{0x}y^2. \end{aligned} \tag{14}$$

The solutions (13) and the stress function form (14) are substituted into Eq. (10), and the like-Galerkin method can be applied for the shallow panels, the coefficients of Eq. (14) are obtained by

$$\begin{aligned} \varphi_1 &= \bar{x}_{11}\left(W + 2\kappa h\right)W + \bar{x}_{12}W,\\ \varphi_2 &= \bar{x}_{21}\left(W + 2\kappa h\right)W + \bar{x}_{22}W,\\ \varphi_3 &= \bar{x}_{31}\Phi_x + \bar{x}_{32}\Phi_y + \bar{x}_{33}W, \end{aligned} \tag{15}$$

where the coefficients $\bar{x}_{ij}$ are presented in Appendix A.

The average expressions of immovable conditions for the edges can be presented as

$$\begin{aligned} &\int_0^b\int_0^a u_{,x}dxdy = \bar{y}_{41}W + \bar{y}_{42}\Phi_x + \bar{y}_{43}\Phi_y + \bar{y}_{47}\Delta T\\ &+\bar{y}_{44}W\left(2\kappa h + W\right) + \bar{y}_{45}N_{0x} + \bar{y}_{46}N_{0y} = 0, \end{aligned} \tag{16}$$

$$\begin{aligned} &\int_0^b\int_0^a v_{,y}dxdy = \bar{y}_{51}W + \bar{y}_{52}\Phi_x + \bar{y}_{53}\Phi_y + \bar{y}_{57}\Delta T\\ &+\bar{y}_{54}W\left(2\kappa h + W\right) + \bar{y}_{55}N_{0x} + \bar{y}_{56}N_{0y} = 0, \end{aligned} \tag{17}$$

where the coefficients $\bar{y}_{ij}$ are presented in Appendix B.

The strain energy of the panel, the work done by the external loads, and the kinetic energy, considering the system damping, are calculated as

$$\begin{aligned} \bar{\Upsilon}_{in} &= \frac{1}{2}\int_{-h/2}^{h/2}\int_0^b\int_0^a\left(\sigma_{xz}\gamma_{xz} + \sigma_{xy}\gamma_{xy} + \sigma_{yz}\gamma_{yz}\right)dxdydz\\ &+\frac{1}{2}\int_{-h/2}^{h/2}\int_0^b\int_0^a\begin{bmatrix}\sigma_x\left(\varepsilon_x - \alpha_{11}\Delta T\right)\\ +\sigma_y\left(\varepsilon_y - \alpha_{22}\Delta T\right)\end{bmatrix}dxdydz. \end{aligned} \tag{18}$$

$$\bar{\Upsilon}_{ext} = \int_0^b\int_0^a qwdxdy. \tag{19}$$

$$\bar{\Upsilon}_t = \frac{1}{2}\int_{-h/2}^{h/2}\int_0^b\int_0^a\rho\left(w_{,t} + \bar{w}_{,t}\right)^2 dxdydz. \tag{20}$$

The Lagrange function can be expressed to obtain the total energy of panel, as

$$\bar{\Upsilon}_{Total} = \bar{\Upsilon}_t - \bar{\Upsilon}_{in} + \bar{\Upsilon}_{ext}. \tag{21}$$

Utilizing the Rayleigh dissipation function, the damping potential function is obtained as

$$d_V = \frac{1}{2}\int_0^b\int_0^a cw_{,t}^2 dxdy. \tag{22}$$

The Euler-Lagrange equations, combined with the Rayleigh dissipation function, can be applied, as

$$\frac{d}{dt}\left(\frac{\partial\bar{\Upsilon}_{Total}}{\partial\dot{W}}\right)-\frac{\partial\bar{\Upsilon}_{Total}}{\partial W}+\frac{\partial d_V}{\partial\dot{W}}=0,$$
$$\frac{d}{dt}\left(\frac{\partial\bar{\Upsilon}_{Total}}{\partial\dot{\Phi}_x}\right)-\frac{\partial\bar{\Upsilon}_{Total}}{\partial\Phi_x}=0, \quad (23)$$
$$\frac{d}{dt}\left(\frac{\partial\bar{\Upsilon}_{Total}}{\partial\dot{\Phi}_y}\right)-\frac{\partial\bar{\Upsilon}_{Total}}{\partial\Phi_y}=0,$$

leads to

$$\begin{aligned}&\bar{y}_{11}W+\bar{y}_{12}\Phi_x+\bar{y}_{13}\Phi_y\\&+(W+\kappa h)(\bar{y}_{14}\Phi_x+\bar{y}_{15}\Phi_y)\\&+(W+\kappa h)\left[\bar{y}_{17}W(W+2\kappa h)+\bar{y}_{19}N_{0x}\right]\\&+\bar{y}_{16}W(W+4/3\,\kappa h)+\bar{y}_{18}N_{0x}+\bar{y}_{110}N_{0y}\\&-\bar{y}_{112}q-\bar{y}_{113}\Delta T+\bar{y}_{115}\ddot{W}+\bar{y}_{116}c\dot{W}=0,\end{aligned} \quad (24)$$

$$\begin{aligned}&\bar{y}_{12}W+\bar{y}_{22}\Phi_x+\bar{y}_{23}\Phi_y+\bar{y}_{24}W(W+2\kappa h)\\&+\bar{y}_{25}N_{0x}+\bar{y}_{26}N_{0y}-\bar{y}_{27}\Delta T=0,\end{aligned} \quad (25)$$

$$\begin{aligned}&\bar{y}_{13}W+\bar{y}_{23}\Phi_x+\bar{y}_{33}\Phi_y+\bar{y}_{34}W(W+2\kappa h)\\&+\bar{y}_{35}N_{0x}+\bar{y}_{36}N_{0y}-\bar{y}_{37}\Delta T=0,\end{aligned} \quad (26)$$

where the coefficients $\bar{y}_{ij}$ are presented in Appendix B.

The motion equation is obtained by using Eqs. (24-26), and combining with $N_{0x}=0$ and $N_{0y}=0$ for 4F boundary condition, with Eqs. (16) and (17), presented as

$$\begin{aligned}&(\vartheta_1\bar{\varsigma}_{11}+\vartheta_2\bar{\varsigma}_{41})W+(\vartheta_1\bar{\varsigma}_{110}+\vartheta_2\bar{\varsigma}_{46})\Delta T\\&+(\kappa h+W)(\vartheta_1\bar{\varsigma}_{12}+\vartheta_2\bar{\varsigma}_{42})\Delta T\\&+(\kappa h+W)(\vartheta_1\bar{\varsigma}_{13}+\vartheta_2\bar{\varsigma}_{43})W\\&+(2\kappa h+W)(\vartheta_1\bar{\varsigma}_{12}+\vartheta_4\bar{\varsigma}_{44})W\\&+(2\kappa h+W)(\vartheta_1\bar{\varsigma}_{15}+\vartheta_2\bar{\varsigma}_{45})W(W+\kappa h)\\&+\bar{\Upsilon}_{16}W(W+4\kappa h/3)-\bar{\Upsilon}_{112}q\\&+\bar{\Upsilon}_{115}\ddot{W}+\bar{\Upsilon}_{116}c\dot{W}=0,\end{aligned} \quad (27)$$

where, $\vartheta_1=1,\ \vartheta_2=0$ for the case of the 4F condition, $\vartheta_1=0,\ \vartheta_2=1$ for the case of 4I, and

$$\bar{\varsigma}_{11}=\bar{y}_{12}\bar{o}_{14}+\bar{y}_{13}\bar{o}_{24}+\bar{y}_{11},\ \bar{\varsigma}_{12}=\bar{y}_{14}\bar{o}_{15}+\bar{y}_{15}\bar{o}_{25},$$
$$\bar{\varsigma}_{13}=\bar{y}_{14}\bar{o}_{14}+\bar{y}_{15}\bar{o}_{24},\ \bar{\varsigma}_{14}=\bar{y}_{12}\bar{o}_{11}+\bar{y}_{15}\bar{o}_{24},$$
$$\bar{\varsigma}_{15}=\bar{y}_{14}\bar{o}_{11}+\bar{y}_{15}\bar{o}_{21}+\bar{y}_{17},\ \bar{\varsigma}_{16}=\bar{y}_{12}\bar{o}_{13}+\bar{y}_{13}\bar{o}_{23}+\bar{y}_{18},$$
$$\bar{\varsigma}_{17}=\bar{y}_{14}\bar{o}_{13}+\bar{y}_{15}\bar{o}_{23}+\bar{y}_{19},\ \bar{\varsigma}_{18}=\bar{y}_{12}\bar{o}_{12}+\bar{y}_{13}\bar{o}_{22}+\bar{y}_{110},$$
$$\bar{\varsigma}_{19}=\bar{y}_{14}\bar{o}_{12}+\bar{y}_{15}\bar{o}_{22},\ \bar{\varsigma}_{110}=\bar{y}_{12}\bar{o}_{15}+\bar{y}_{13}\bar{o}_{25}-\bar{y}_{113},$$

$$\bar{\varsigma}_{41}=\bar{\varsigma}_{11}-\frac{\bar{\varsigma}_{16}(\bar{o}_{32}\bar{o}_{43}+\bar{o}_{42})+\bar{\varsigma}_{18}(\bar{o}_{33}\bar{o}_{42}+\bar{o}_{32})}{\bar{o}_{33}\bar{o}_{43}-1},$$

$$\bar{\varsigma}_{42}=\bar{\varsigma}_{12}-\frac{\bar{\varsigma}_{17}(\bar{o}_{34}\bar{o}_{43}+\bar{o}_{44})+\bar{\varsigma}_{19}(\bar{o}_{33}\bar{o}_{44}+\bar{o}_{34})}{\bar{o}_{33}\bar{o}_{43}-1},$$

$$\bar{\varsigma}_{43}=\bar{\varsigma}_{13}-\frac{\bar{\varsigma}_{17}(\bar{o}_{32}\bar{o}_{43}+\bar{o}_{42})+\bar{\varsigma}_{19}(\bar{o}_{33}\bar{o}_{42}+\bar{o}_{32})}{\bar{o}_{33}\bar{o}_{43}-1},$$

$$\bar{\varsigma}_{44}=\bar{\varsigma}_{14}-\frac{\bar{\varsigma}_{16}(\bar{o}_{31}\bar{o}_{43}+\bar{o}_{41})+\bar{\varsigma}_{18}(\bar{o}_{33}\bar{o}_{41}+\bar{o}_{31})}{\bar{o}_{33}\bar{o}_{43}-1},$$

$$\bar{\varsigma}_{45}=\bar{\varsigma}_{15}-\frac{\bar{\varsigma}_{17}(\bar{o}_{31}\bar{o}_{43}+\bar{o}_{41})+\bar{\varsigma}_{19}(\bar{o}_{33}\bar{o}_{41}+\bar{o}_{31})}{\bar{o}_{33}\bar{o}_{43}-1},$$

$$\bar{\varsigma}_{46}=\bar{\varsigma}_{110}-\frac{\bar{\varsigma}_{16}(\bar{o}_{34}\bar{o}_{43}+\bar{o}_{44})+\bar{\varsigma}_{18}(\bar{o}_{33}\bar{o}_{44}+\bar{o}_{34})}{\bar{o}_{33}\bar{o}_{43}-1},$$

$$\bar{o}_{11}=\frac{\bar{y}_{33}\bar{y}_{24}-\bar{y}_{34}\bar{y}_{23}}{-\bar{y}_{22}\bar{y}_{33}+\bar{y}_{23}^2},\ \bar{o}_{12}=-\frac{\bar{y}_{23}\bar{y}_{36}-\bar{y}_{33}\bar{y}_{26}}{-\bar{y}_{22}\bar{y}_{33}+\bar{y}_{23}^2},$$
$$\bar{o}_{13}=-\frac{\bar{y}_{35}\bar{y}_{23}-\bar{y}_{33}\bar{y}_{25}}{-\bar{y}_{22}\bar{y}_{33}+\bar{y}_{23}^2},\bar{o}_{14}=-\frac{-\bar{y}_{33}\bar{y}_{12}+\bar{y}_{13}\bar{y}_{23}}{-\bar{y}_{22}\bar{y}_{33}+\bar{y}_{23}^2},$$
$$\bar{o}_{15}=\frac{\bar{y}_{37}\bar{y}_{23}-\bar{y}_{33}\bar{y}_{27}}{-\bar{y}_{22}\bar{y}_{33}+\bar{y}_{23}^2},\ \bar{o}_{16}=\frac{\bar{y}_{38}\bar{y}_{23}-\bar{y}_{33}\bar{y}_{28}}{-\bar{y}_{22}\bar{y}_{33}+\bar{y}_{23}^2},$$

$$\bar{o}_{21}=-\frac{-\bar{y}_{34}\bar{y}_{22}+\bar{y}_{23}\bar{y}_{24}}{-\bar{y}_{22}\bar{y}_{33}+\bar{y}_{23}^2},$$

$$\bar{o}_{22}=\frac{\bar{y}_{36}\bar{y}_{22}-\bar{y}_{23}\bar{y}_{26}}{-\bar{y}_{22}\bar{y}_{33}+\bar{y}_{23}^2},$$

$$\bar{o}_{23}=\frac{-\bar{y}_{23}\bar{y}_{25}+\bar{y}_{35}\bar{y}_{23}}{-\bar{y}_{22}\bar{y}_{33}+\bar{y}_{23}^2},$$

$$\bar{o}_{24}=\frac{-\bar{y}_{12}\bar{y}_{23}+\bar{y}_{13}\bar{y}_{22}}{-\bar{y}_{22}\bar{y}_{33}+\bar{y}_{23}^2},$$

$$\bar{o}_{25}=\frac{-\bar{y}_{22}\bar{y}_{37}+\bar{y}_{23}\bar{y}_{27}}{-\bar{y}_{22}\bar{y}_{33}+\bar{y}_{23}^2},$$

$$\bar{o}_{26}=\frac{-\bar{y}_{22}\bar{y}_{38}+\bar{y}_{23}\bar{y}_{28}}{-\bar{y}_{22}\bar{y}_{33}+\bar{y}_{23}^2},$$

$$\bar{o}_{31}=-\frac{\bar{y}_{52}\bar{o}_{11}+\bar{y}_{53}\bar{o}_{21}+\bar{y}_{54}}{\bar{y}_{52}\bar{o}_{12}+\bar{y}_{53}\bar{o}_{22}+\bar{y}_{56}},$$

$$\bar{o}_{32}=-\frac{\bar{y}_{52}\bar{o}_{14}+\bar{y}_{53}\bar{o}_{24}+\bar{y}_{51}}{\bar{y}_{52}\bar{o}_{12}+\bar{y}_{53}\bar{o}_{22}+\bar{y}_{56}},$$

$$\bar{o}_{33}=-\frac{\bar{y}_{52}\bar{o}_{13}+\bar{y}_{53}\bar{o}_{23}+\bar{y}_{55}}{\bar{y}_{52}\bar{o}_{12}+\bar{y}_{53}\bar{o}_{22}+\bar{y}_{56}},$$

$$\bar{o}_{34} = -\frac{\bar{y}_{52}\bar{o}_{15} + \bar{y}_{53}\bar{o}_{25} + \bar{y}_{57}}{\bar{y}_{52}\bar{o}_{12} + \bar{y}_{53}\bar{o}_{22} + \bar{y}_{56}},$$

$$\bar{o}_{35} = -\frac{\bar{y}_{52}\bar{o}_{16} + \bar{y}_{53}\bar{o}_{26} + \bar{y}_{58}}{\bar{y}_{52}\bar{o}_{12} + \bar{y}_{53}\bar{o}_{22} + \bar{y}_{56}},$$

$$\bar{o}_{41} = -\frac{\bar{o}_{11}\bar{y}_{42} + \bar{o}_{21}\bar{y}_{43} + \bar{y}_{44}}{\bar{o}_{13}\bar{y}_{42} + \bar{o}_{23}\bar{y}_{43} + \bar{y}_{45}},$$

$$\bar{o}_{42} = -\frac{\bar{o}_{14}\bar{y}_{42} + \bar{o}_{24}\bar{y}_{43} + \bar{y}_{41}}{\bar{o}_{13}\bar{y}_{42} + \bar{o}_{23}\bar{y}_{43} + \bar{y}_{45}},$$

$$\bar{o}_{43} = -\frac{\bar{o}_{12}\bar{y}_{42} + \bar{o}_{22}\bar{y}_{43} + \bar{y}_{46}}{\bar{o}_{13}\bar{y}_{42} + \bar{o}_{23}\bar{y}_{43} + \bar{y}_{45}},$$

$$\bar{o}_{44} = -\frac{\bar{o}_{15}\bar{y}_{42} + \bar{o}_{25}\bar{y}_{43} + \bar{y}_{47}}{\bar{o}_{13}\bar{y}_{42} + \bar{o}_{23}\bar{y}_{43} + \bar{y}_{45}},$$

$$\bar{o}_{45} = -\frac{\bar{o}_{16}\bar{y}_{42} + \bar{o}_{26}\bar{y}_{43} + \bar{y}_{48}}{\bar{o}_{13}\bar{y}_{42} + \bar{o}_{23}\bar{y}_{43} + \bar{y}_{45}}.$$

The motion equation of free and linear vibration can be obtained by eliminating the nonlinearities and loading term components. From that, the frequency of free and linear vibration can be obtained as

$$\omega_{mn} = \sqrt{\frac{\vartheta_1\bar{\varsigma}_{11} + \vartheta_2\bar{\varsigma}_{41} + (\vartheta_1\bar{\varsigma}_{12} + \vartheta_2\bar{\varsigma}_{42})\Delta T}{\bar{y}_{115}}}. \quad (28)$$

Two forms of impulse loads are considered in this paper, including finite duration step and triangular blast loads, with the following functions, respectively, as (29)

$$q(t) = \begin{cases} \begin{cases} Q\left(1 - \dfrac{t}{T}\right), 0 \le t \le T \\ 0, \quad t > T \end{cases} & \text{Triangular blast load} \\ \begin{cases} Q, \quad 0 \le t \le T \\ 0, \quad t > T \end{cases} & \text{Finite duration step load} \end{cases}$$

where $T = \dfrac{2\pi}{\omega_{mn}}$ is the vibration period.

Substituting the impulse load types in the Eq. (29) into Eq. (27), and the Runge-Kutta method is applied to obtain the dynamic responses of panels. The initial conditions are assumed to be zero, meaning the panel is initially at rest. Specifically, both the initial deflection and initial velocity are taken as zero

$$W\big|_{t=0} = 0, \ \dot{W}\big|_{t=0} = 0, \quad (30)$$

5. Results and discussions

Table 1 presents a validation study of the fundamental frequency parameters of FG-GRC cylindrical panels with various graphene distribution types at different temperatures. The present results are compared with those reported by Shen et al. [26] for the $(0/90/0/90/0)_S$ lay-up configuration under 4F boundary conditions. As shown in the table, an excellent agreement is observed between the present semi-analytical approach and the reference data across all investigated cases, with relative differences being negligibly small. This consistency confirms the accuracy and reliability of the developed formulation in predicting the dynamic behavior of functionally graded graphene-reinforced panels.

Table 2 illustrates the effects of graphene arrangement, panel geometry, and graphene distribution law on the fundamental frequencies of FG-GRMMC panels. Three lay-up schemes, $(0)_{10}$, $(0/90)_{5T}$, and $(0/90/0/90/0)_S$, are examined across three geometric configurations: cylindrical, parabolic, and sinusoidal panels. For each case, five graphene distribution laws (UD, FG-X, FG-O, FG-V, and FG-Λ) are considered. A consistent trend observed across all configurations is that the FG-X distribution yields the highest fundamental frequencies, while the FG-O configuration results in the lowest values. This is consistent with the earlier observations in Table 1 and is attributed to the placement of stiffer graphene-rich layers near the outer surfaces in FG-X, which enhances the bending rigidity. In contrast, the FG-O distribution concentrates stiffer material closer to the mid-plane, reducing the eccentricity and thereby lowering the flexural stiffness. Regarding panel geometry, the differences in frequency values among the cylindrical, parabolic, and sinusoidal panels are minimal for the same material

configuration. This suggests that, under the assumed shallow curvature conditions, the influence of curvature type on the fundamental frequency is secondary compared to the material distribution and lay-up scheme. Additionally, the effect of fiber orientation is found to be relatively small, as indicated by the close proximity of frequency values among the three lay-up types.

Table 1. Validation of the fundamental frequency parameters $\tilde{\omega}_{mn} = \omega_{mn}\left(a^2/h\right)\sqrt{\rho_0/E_0}$ of $(0/90/0/90/0)_S$ FG-GRC cylindrical panels (4F, $a/b = 1$, $h = 2$ mm, $a/R_{(c)} = 0.5$, $b/h = 20$, $m = n = 1$)

T (K)	Distribution	Shen et al. [26]	Present
300	UD	38.0071	38.0804
	FG-X	39.5231	39.6005
	FG-V	34.6249	34.6964
	FG-Λ	36.2314	36.3017
	FG-O	33.8763	33.9400
400	UD	35.3452	35.4113
	FG-X	36.4831	36.5527
	FG-V	32.7796	32.8433
	FG-Λ	33.3561	33.1578
	FG-O	31.4769	31.5344

Table 2. Effects of graphene arrangements, panel configurations and graphene distribution laws on the fundamental frequencies (rad/s) of FG-GRMMC panels (4F, h =3mm, $a = b = 20h$, $H = 0.5h$, κ =0, ΔT = 200K, $m = n = 1$)

		UD	FG-X	FG-O	FG-V	FG-Λ
$(0)_{10}$	Sinusoid	24213.88	25675.37	22476.88	23546.84	23867.01
	Parabolic	24206.12	25668.02	22468.50	23538.48	23859.46
	Cylindrical	24206.16	25668.05	22468.53	23538.51	23859.49
$(0/90)_{5T}$	Sinusoid	24213.79	25675.33	22476.86	23546.38	23867.33
	Parabolic	24206.52	25668.40	22468.94	23538.47	23860.23
	Cylindrical	24206.56	25668.44	22468.98	23538.51	23860.27
$(0/90/0/90/0)_S$	Sinusoid	24214.03	25675.33	22476.83	23545.79	23865.72
	Parabolic	24206.66	25668.41	22468.93	23537.78	23858.51
	Cylindrical	24206.70	25668.45	22468.97	23537.81	23858.55

Table 3 presents the variation of fundamental frequencies of sinusoidal FG-GRMMC panels with temperature, considering different graphene distribution laws under (4I) boundary conditions and the $(0)_{10}$ lay-up. The analysis is performed at four distinct temperature levels: 0 K, 200 K, 400 K, and 700 K. As expected, a clear decreasing trend in the fundamental frequency is observed as the temperature increases for all graphene distributions. This reduction is attributed to the temperature dependence of the material properties, particularly the elastic moduli of both

the copper matrix and graphene reinforcement, which degrade at elevated temperatures, thereby reducing the overall stiffness of the considered structures.

Table 3. Effects of temperature changes on the fundamental frequencies (rad/s) of FG-GRMMC sinusoid panels ($(0)_{10}$, 4l, h =3mm, a = b = 20h, H = 0.5h, κ =0, m = n = 1)

ΔT(K)	0	200	400	700
UD	25608.99	24481.35	23321.07	21294.38
FG-X	27216.55	25951.96	25022.88	22828.31
FG-O	23972.63	22792.33	21616.64	19485.38
FG-V	24975.91	23763.53	22716.56	20439.19
FG-Λ	25440.13	24163.77	23153.42	20951.36

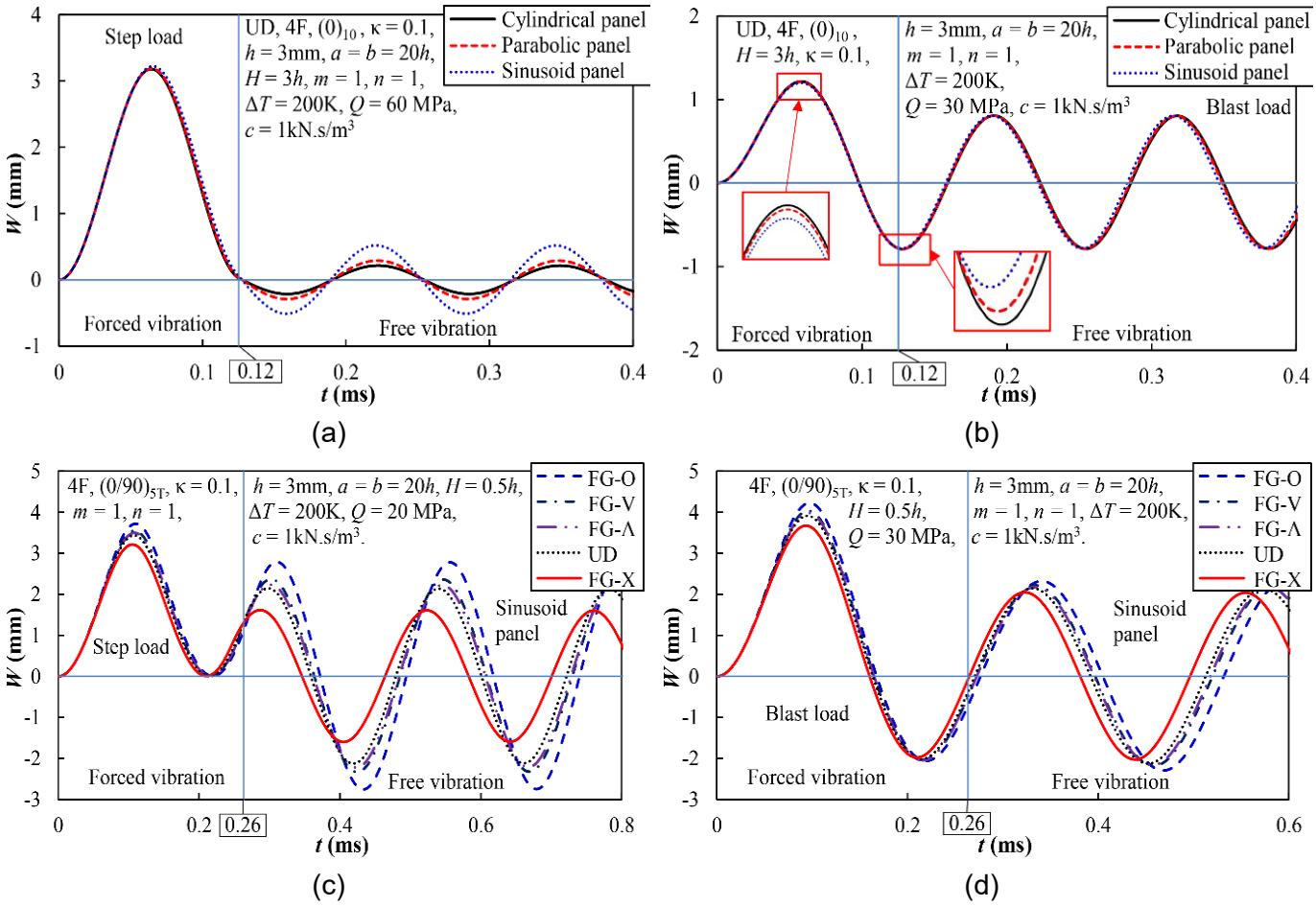

Fig. 2. Effects of panel configurations, and graphene distribution laws on the dynamic responses of FG-GRMMC panels

Fig. 2 presents the time-history deflection responses of FG-GRMMC panels under step and blast impulsive loads. The figure is divided into four subfigures: Figs. 2(a) and 2(b) show the effect of panel geometry (cylindrical, parabolic, and sinusoidal) under step and blast loads, respectively, while Fig. 2(c) and 2(d) illustrate the influence of different graphene distribution laws under the same loading types. A vertical blue line is used in each subplot to indicate the moment at which the external load is removed, thus separating the loading phase from the post-loading phase. In the loading phase, prior to the blue line, the responses of all panel geometries appear

relatively similar, with only slight differences in peak deflection. However, clear distinctions emerge in the post-loading phase, where the structure oscillates freely in response. Notably, sinusoidal panels exhibit the largest amplitude; in contrast, cylindrical panels show the smallest post-loading amplitude. Figs. 2(c) and 2(d) reveal the sensitivity of the system to graphene distribution patterns. FG-X and UD panels consistently demonstrate smaller deflection amplitudes, highlighting the advantage of placing graphene-rich layers near the outer surfaces. Conversely, FG-O distributions lead to larger amplitudes. These effects are especially pronounced in the step load case.

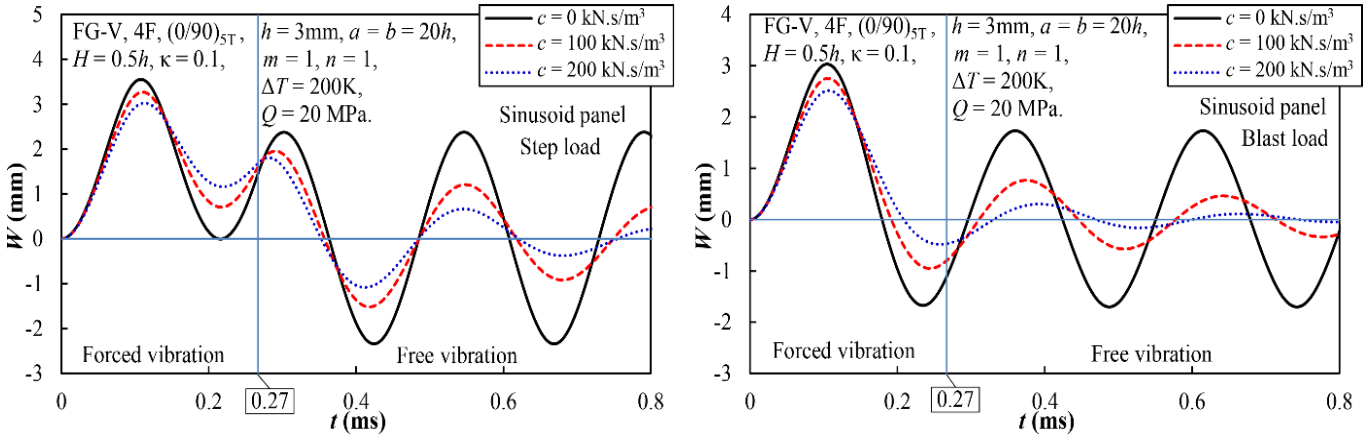

Fig. 3. Effects of damping coefficients on the dynamic responses of FG-GRMMC sinusoid panels

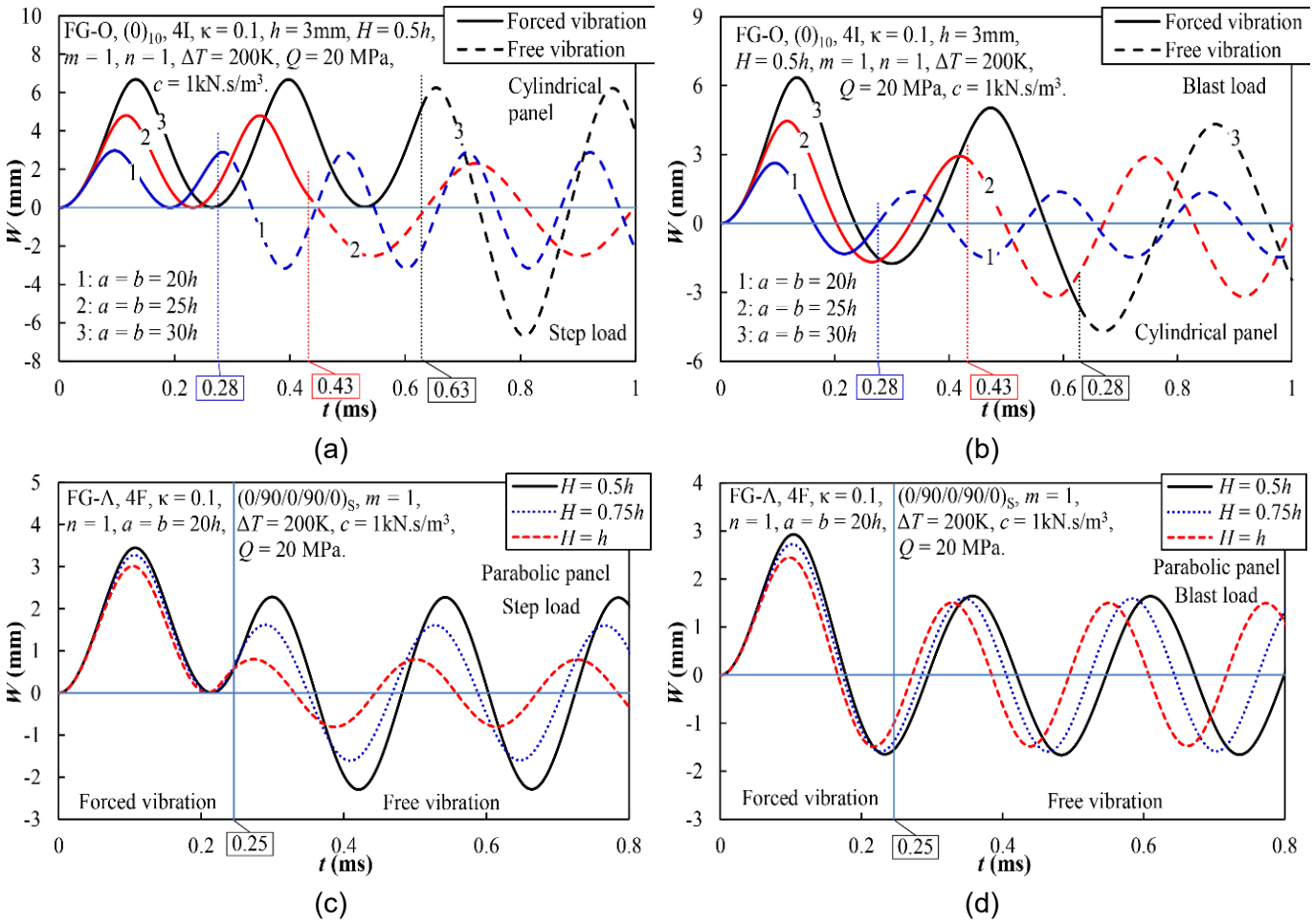

Fig. 4. Effects of geometrical parameters on the dynamic responses of FG-GRMMC panels

Fig. 3 illustrates the effect of the damping coefficient on the dynamic response of sinusoidal FG-GRMMC panels subjected to step load (Fig. 3(a)) and blast load (Fig. 3(b)). Various levels of viscous damping are considered to investigate how energy dissipation influences the time-history deflection behavior under impulsive excitation. As observed in both subplots, increasing the damping coefficient leads to a significant reduction in vibration amplitude and a faster attenuation of oscillations in the post-loading phase. Panels with low damping exhibit pronounced and sustained oscillations after the external load is removed, whereas higher damping results in rapid stabilization and lower peak responses. This trend is consistent across both loading types. Another important observation is that the post-loading oscillation amplitudes in the case of blast loading are consistently lower than those observed under step loading, even when the damping coefficient is held constant. This difference underscores the role of energy input duration.

Fig. 4 explores the influence of key geometrical parameters on the nonlinear dynamic responses of FG-GRMMC panels subjected to impulsive loading. Figs. 4(a) and 4(b) show the effect of edge length under step and blast loads, respectively, while Figs. 4(c) and 4(d) illustrate the effect of panel rise (geometrical curvature) under the same loading types. In Figs. 4(a) and 4(b), it is evident that increasing the panel's edge length leads to larger deflection amplitudes. Longer panels possess lower global stiffness and reduced bending resistance, making them more susceptible to deformation under dynamic excitation. The trend holds for both loading types, although the magnitude of deflection is generally lower under blast loading due to its shorter energy application duration, as previously discussed. Figs. 4(c) and 4(d) demonstrate the significant effect of panel rise. As the rise increases, the panels exhibit markedly smaller deflections and faster decay rates after the load is removed. This behavior is attributed to the increased geometric stiffness provided by the curvature, which enhances the structural resistance against impulses.

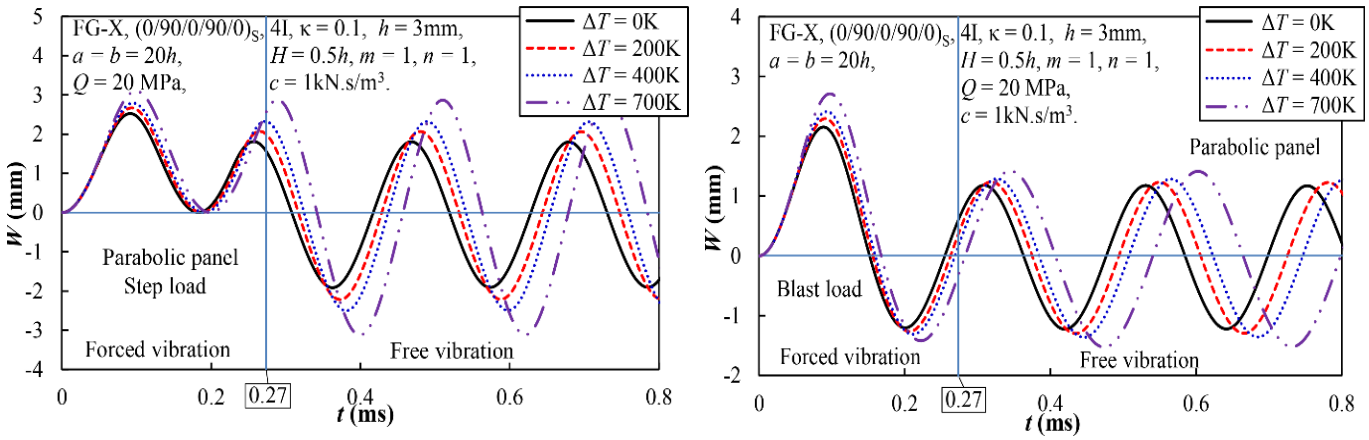

(a) (b)

Fig. 5. Effects of temperature changes on the dynamic responses of FG-GRMMC parabolic panels

Fig. 5 illustrates the influence of temperature variation on the dynamic responses of parabolic FG-GRMMC panels subjected to step load (Fig. 5(a)) and blast loads (Fig. 5(b)). Four temperature levels are considered, and the corresponding time-history deflections are compared to assess the thermal sensitivity of the panel under impulsive excitation. In both loading scenarios, a consistent trend is observed: as the temperature increases, the maximum deflection increases and the system exhibits more prolonged oscillations in the post-loading phase. This behavior is attributed to the

temperature-dependent degradation of material stiffness, particularly in the copper matrix. At elevated temperatures, the elastic modulus of the composite decreases, resulting in reduced bending resistance and increased susceptibility to deformation under the same external impulse.

6. Conclusion

This study proposed a semi-analytical framework to investigate the nonlinear dynamic behavior of FG-GRMMC panels with complex curvatures under impulsive loads and thermal environments. The HSDT combined with von Kármán-type geometric nonlinearities was employed, and the governing equations were derived via the energy approach using the Euler–Lagrange principle. A like-Galerkin approximation was used to satisfy the compatibility condition, and numerical integration was carried out via the Runge–Kutta method. Key findings of this research can be summarized as follows:

1. Among the three configurations studied, sinusoidal panels consistently exhibited the largest post-loading deflections, while cylindrical panels displayed the smallest.

2. The FG-X distribution, which places graphene-rich layers near the outer surfaces, leads to higher stiffness and lower deflection amplitudes compared to other distribution patterns, especially FG-O.

3. Damping effects were found to significantly suppress vibration amplitudes, with higher damping coefficients resulting in faster decay of oscillations.

4. Increasing the panel length amplified deflections, while increasing curvature reduced deformation, reflecting the structural stiffening effect of geometric form.

5. As temperature increased, deflection amplitudes grew larger and vibrational decay became slower, highlighting the necessity of incorporating temperature-dependent material properties in design.

6. The findings of this study offer valuable insights for the design of advanced structural components subjected to impulsive loads. The proposed framework can be effectively applied in engineering applications such as aerospace structures, defense systems, and high-performance thermal shielding where lightweight curved panels with enhanced dynamic carrying capacity are required.

References

[1] B.A.S. Shariat, R. Javaheri, M.R. Eslami. (2005). Buckling of imperfect functionally graded plates under in-plane compressive loading. *Thin-Walled Structures*, 43(7), 1020-1036. https://doi.org/10.1016/j.tws.2005.01.002

[2] B.A.S. Shariat, M.R. Eslami. (2007). Buckling of thick functionally graded plates under mechanical and thermal loads. *Composite Structures*, 78(3), 433-439. https://doi.org/10.1016/j.tws.2005.01.002

[3] H.S. Shen, S.R. Li. (2008). Postbuckling of sandwich plates with FGM face sheets and temperature-dependent properties. *Composites Part B: Engineering*, 39(2), 332-344. https://doi.org/10.1016/j.compositesb.2007.01.004

[4] H.S. Shen. (2007). Thermal postbuckling behavior of shear deformable FGM plates with temperature-dependent properties. *International Journal of Mechanical Sciences*, 49(4), 466-478. https://doi.org/10.1016/j.ijmecsci.2006.09.011

[5] V.H. Nam, D.T. Dong, N.T. Phuong, H.D. Tuan. (2019). Nonlinear thermo-mechanical stability of multilayer-FG plates reinforced by orthogonal and oblique stiffeners according to FSDT. *Journal of Reinforced Plastics and Composites*, 38(11), 521-536. https://doi.org/10.1177/0731684419831650

[6] V.H. Nam, N.T. Phuong, D.T. Dong, N.T. Trung, N.V. Tue. (2019). Nonlinear thermo-mechanical

buckling of higher-order shear deformable porous functionally graded material plates reinforced by orthogonal and/or oblique stiffeners. *Proceedings of the Institution of Mechanical Engineers, Part C: Journal of Mechanical Engineering Science*, 233(17), 6177-6196. https://doi.org/10.1177/0954406219861658

[7] D.T. Dong, V.H. Nam, N.T. Trung, N.T. Phuong, V.T. Hung. (2022). Nonlinear thermomechanical buckling of sandwich FGM oblique stiffened plates with nonlinear effect of elastic foundation. *Journal of Thermoplastic Composite Materials*, 35(10), 1441-1467. https://doi.org/10.1177/0892705720935957

[8] L.W. Zhang, W.C. Cui, K.M. Liew. (2015). Vibration analysis of functionally graded carbon nanotube reinforced composite thick plates with elastically restrained edges. *International Journal of Mechanical Sciences*, 103, 9-21. https://doi.org/10.1016/j.ijmecsci.2015.08.021

[9] L.W. Zhang, Z.G. Song, K.M. Liew. (2015). Nonlinear bending analysis of FG-CNT reinforced composite thick plates resting on Pasternak foundations using the element-free IMLS-Ritz method. *Composite Structures*, 128, 165-175. https://doi.org/10.1016/j.compstruct.2015.03.011

[10] L.W. Zhang, Z.X. Lei, K.M. Liew. (2015). Buckling analysis of FG-CNT reinforced composite thick skew plates using an element-free approach. *Composites Part B: Engineering*, 75, 36-46. https://doi.org/10.1016/j.compositesb.2015.01.033

[11] L.W. Zhang, K.M. Liew. (2015). Geometrically nonlinear large deformation analysis of functionally graded carbon nanotube reinforced composite straight-sided quadrilateral plates. *Computer Methods in Applied Mechanics and Engineering*, 295, 219-239. https://doi.org/10.1016/j.cma.2015.07.006

[12] L.W. Zhang, K.M. Liew. (2015). Large deflection analysis of FG-CNT reinforced composite skew plates resting on Pasternak foundations using an element-free approach. *Composite Structures*, 132, 974-983. https://doi.org/10.1016/j.compstruct.2015.07.017

[13] L.W. Zhang, K.M. Liew. (2016). Postbuckling analysis of axially compressed CNT reinforced functionally graded composite plates resting on Pasternak foundations using an element-free approach. *Composite Structures*, 138, 40-51. https://doi.org/10.1016/j.compstruct.2015.11.031

[14] J. Yang, X.H. Huang, H.-S. Shen. (2020). Nonlinear vibration of temperature-dependent FG-CNTRC laminated plates with negative Poisson's ratio. *Thin-Walled Structures*, 148, 106514.https://doi.org/10.1016/j.tws.2019.106514

[15] R. Bellman, B.G. Kashef, J. Casti. (1972). Differential quadrature: A technique for the rapid solution of nonlinear partial differential equations. *Journal of Computational Physics*, 10, 40-52. https://doi.org/10.1016/0021-9991(72)90089-7

[16] A. Alibeigloo, A. Emtehani. (2015). Static and free vibration analyses of carbon nanotube-reinforced composite plate using differential quadrature method. *Meccanica*, 50, 61-76. https://doi.org/10.1007/s11012-014-0050-7

[17] P. Jiao, Z. Chen, H. Ma, D. Zhang, P. Ge. (2019). Buckling analysis of thin rectangular FG-CNTRC plate subjected to arbitrarily distributed partial edge compression loads based on differential quadrature method. *Thin-Walled Structures*, 145, 106417. https://doi.org/10.1016/j.tws.2019.106417

[18] Y. Kiani, M. Mirzaei. (2018). Rectangular and skew shear buckling of FG-CNT reinforced composite skew plates using Ritz method. *Aerospace Science and Technology*, 77, 388-398. https://doi.org/10.1016/j.ast.2018.03.022

[19] Y. Kiani. (2016). Shear buckling of FG-CNT reinforced composite plates using Chebyshev-Ritz method. *Composites Part B: Engineering*, 105, 176-187. https://doi.org/10.1016/j.compositesb.2016.09.001

[20] Y. Kiani. (2017). Dynamics of FG-CNT reinforced composite cylindrical panel subjected to moving load. *Thin-Walled Structures*, 111, 48-57. https://doi.org/10.1016/j.tws.2016.11.011

[21] K. Foroutan, H. Ahmadi, E. Carrera. (2019). Nonlinear vibration of imperfect FG-CNTRC cylindrical panels under external pressure in the thermal environment. *Composite Structures*, 227, 111310. https://doi.org/10.1016/j.compstruct.2019.111310

[22] K. Foroutan, E. Carrera, H. Ahmadi. (2020). Nonlinear hygrothermal vibration and buckling analysis of imperfect FG-CNTRC cylindrical panels embedded in viscoelastic foundations. *European Journal of Mechanics - A/Solids*, 85, 104107. https://doi.org/10.1016/j.euromechsol.2020.104107

[23] H.S. Shen, Y. Xiang, F. Lin, D. Hui. (2017). Buckling and postbuckling of functionally graded graphene-reinforced composite laminated plates in thermal environments. *Composites Part B: Engineering*, 119, 67-78. https://doi.org/10.1016/j.compositesb.2017.03.020

[24] H.S. Shen, Y. Xiang, Y. Fan. (2018). Postbuckling of functionally graded graphene-reinforced composite laminated cylindrical panels under axial compression in thermal environments. *International Journal of Mechanical Sciences*, 135, 398-409. https://doi.org/10.1016/j.ijmecsci.2017.11.031

[25] H.S. Shen, Y. Xiang, J.N. Reddy. (2019). Thermal postbuckling behavior of FG-GRC laminated cylindrical panels with temperature-dependent properties. *Composite Structures*, 211, 433-442. https://doi.org/10.1016/j.compstruct.2018.12.023

[26] H.S. Shen, Y. Xiang, Y. Fan, D. Hui. (2018). Nonlinear vibration of functionally graded graphene-reinforced composite laminated cylindrical panels resting on elastic foundations in thermal environments. *Composites Part B: Engineering*, 136, 177-186. https://doi.org/10.1016/j.compositesb.2017.10.032

[27] H.S. Shen, Y. Xiang, Y. Fan. (2019). A novel technique for nonlinear dynamic instability analysis of FG-GRC laminated plates. *Thin-Walled Structures*, 139, 389-397. https://doi.org/10.1016/j.tws.2019.03.010

[28] Y. Kiani. (2018). NURBS-based isogeometric thermal postbuckling analysis of temperature dependent graphene reinforced composite laminated plates. *Thin-Walled Structures*, 125, 211-219. https://doi.org/10.1016/j.tws.2018.01.024

[29] Y. Kiani. (2018). Isogeometric large amplitude free vibration of graphene reinforced laminated plates in thermal environment using NURBS formulation. *Computer Methods in Applied Mechanics and Engineering*, 332, 86-101. https://doi.org/10.1016/j.cma.2017.12.015

[30] Y. Kiani. (2019). Buckling of functionally graded graphene reinforced conical shells under external pressure in thermal environment. *Composites Part B: Engineering*, 156, 128-137. https://doi.org/10.1016/j.compositesb.2018.08.052

[31] N.T. Phuong, D.T. Dong, C.V. Doan, V.H. Nam. (2022). Nonlinear buckling of higher-order shear deformable stiffened FG-GRC laminated plates with nonlinear elastic foundation subjected to combined loads. *Aerospace Science and Technology*, 127, 107736. https://doi.org/10.1016/j.ast.2022.107736

[32] N.T. Phuong, D.T. Dong, C.V. Doan, V.H. Nam. (2023). Nonlinear buckling of stiffened FG-GRCL cylindrical panels under axial compression with the uniformly distributed temperature variation. *The European Physical Journal Plus*, 138(3), 1-15. https://doi.org/10.1140/epjp/s13360-023-03841-5

[33] V.H. Nam, C.V. Doan, N.T. Phuong. (2023). A new analytical approach to the nonlinear buckling and postbuckling behavior of functionally graded graphene reinforced composite laminated cylindrical, parabolic, and half-sinusoid shallow imperfect panels. *Polymer Composites*, 44(12), 8928-8945. https://doi.org/10.1002/pc.27748

[34] N.T. Phuong, V.H. Nam, N.T. Trung, V.M. Duc, N.V. Loi, N.D. Thinh, P.T. Tu. (2021). Thermomechanical postbuckling of functionally graded graphene-reinforced composite laminated toroidal shell segments surrounded by Pasternak's elastic foundation. *Journal of Thermoplastic Composite Materials*, 34(10), 1380-1407. https://doi.org/10.1177/0892705719870593

[35] L.N. Ly, N.T. Phuong, V.H. Nam, N.T. Trung, V.M. Duc. (2020). An Analytical Approach of Nonlinear Thermo-mechanical Buckling of Functionally Graded Graphene-reinforced Composite Laminated Cylindrical Shells under Compressive Axial Load Surrounded by Elastic Foundation. *Journal of Applied and Computational Mechanics*, 6(2), 357-372. https://doi.org/10.22055/jacm.2019.29527.1609

[36] Y. Fan, Y. Xiang, H.S. Shen. (2020). Temperature-Dependent Mechanical Properties of Graphene/Cu Nanocomposites with In-Plane Negative Poisson's Ratios. *Research*, 2020, 5618021. https://doi.org/10.34133/2020/5618021

[37] Y. Fan, H.S. Shen, Y. Xiang. (2023). Nonlinear vibration characteristics of pre- and post-buckled FG-GRMMC laminated plates with in-plane auxeticity. *Engineering Structures*, 274, 115068. https://doi.org/10.1016/j.engstruct.2022.115068

[38] H.S. Shen, Y. Xiang, J.N. Reddy. (2020). Effect of negative Poisson's ratio on the post-buckling behavior of FG-GRMMC laminated plates in thermal environments. *Composite Structures*, 253, 112731. https://doi.org/10.1016/j.compstruct.2020.112731

Appendix A

$$\bar{x}_{11}=\frac{\left(\frac{n\pi}{b}\right)^2}{32\left(\frac{m\pi}{a}\right)^2 e^*_{22}},\quad \bar{x}_{21}=\frac{\left(\frac{m\pi}{a}\right)^2}{32\left(\frac{n\pi}{b}\right)^2 e^*_{11}},\ \ell=\left[(-1)^m-1\right]\left[(-1)^n-1\right],$$

$$\bar{x}_{12}=\frac{8\ell^2\left[\bar{R}_{2(c,p,s)}-\bar{R}_{3(c,p,s)}\right]-12\left(\frac{m\pi}{a}\right)\left(\frac{n\pi}{b}\right)ab\ell\bar{R}_{1(c,p,s)}-9\bar{R}_{2(c,p,s)}a^2b^2\left(\frac{m\pi}{a}\right)^2\left(\frac{n\pi}{b}\right)^2}{72a^3b^3\left(\frac{m\pi}{a}\right)^6\left(\frac{n\pi}{b}\right)^2 e^*_{22}-128ab\left(\frac{m\pi}{a}\right)^4 e^*_{22}\ell^2},$$

$$\bar{x}_{22}=\frac{-8\ell^2\left[\bar{R}_{2(c,p,s)}-\bar{R}_{3(c,p,s)}\right]-12\left(\frac{m\pi}{a}\right)\left(\frac{n\pi}{b}\right)ab\ell\bar{R}_{1(c,p,s)}-9\bar{R}_{3(c,p,s)}a^2b^2\left(\frac{m\pi}{a}\right)^2\left(\frac{n\pi}{b}\right)^2}{72a^3b^3\left(\frac{m\pi}{a}\right)^2\left(\frac{n\pi}{b}\right)^6 e^*_{11}-128ab\left(\frac{n\pi}{b}\right)^4 e^*_{11}\ell^2},$$

$$\bar{x}_{31}=-\frac{\left(\frac{m\pi}{a}\right)\left\{\left[\left(a^*_{66}-a^*_{11}\right)\frac{4}{3h^2}+d^*_{11}-d^*_{66}\right]\left(\frac{n\pi}{b}\right)^2+\left(\frac{m\pi}{a}\right)^2\left(-\frac{4}{3h^2}a^*_{21}+d^*_{21}\right)\right\}}{\left(\frac{m\pi}{a}\right)^4 e^*_{22}+\left(\frac{n\pi}{b}\right)^2\left(2e^*_{12}+e^*_{66}\right)\left(\frac{m\pi}{a}\right)^2+\left(\frac{n\pi}{b}\right)^4 e^*_{11}},$$

$$\bar{x}_{32}=-\frac{\left(\frac{n\pi}{b}\right)\left\{\left[\left(a^*_{66}-a^*_{22}\right)\frac{4}{3h^2}+d^*_{22}-d^*_{66}\right]\left(\frac{m\pi}{a}\right)^2+\left(\frac{n\pi}{b}\right)^2\left(-\frac{4}{3h^2}a^*_{12}+d^*_{12}\right)\right\}}{\left(\frac{m\pi}{a}\right)^4 e^*_{22}+\left(\frac{n\pi}{b}\right)^2\left(2e^*_{12}+e^*_{66}\right)\left(\frac{m\pi}{a}\right)^2+\left(\frac{n\pi}{b}\right)^4 e^*_{11}},$$

$$\bar{x}_{33}=\frac{\frac{4}{3h^2}\left(\frac{m\pi}{a}\right)^4 a^*_{21}+\frac{4}{3h^2}\left(\frac{n\pi}{b}\right)^2\left(a^*_{11}+a^*_{22}-2a^*_{66}\right)\left(\frac{m\pi}{a}\right)^2+\frac{4}{3h^2}\left(\frac{n\pi}{b}\right)^4 a^*_{12}}{\left(\frac{m\pi}{a}\right)^4 e^*_{22}+\left(\frac{n\pi}{b}\right)^2\left(2e^*_{12}+e^*_{66}\right)\left(\frac{m\pi}{a}\right)^2+\left(\frac{n\pi}{b}\right)^4 e^*_{11}}$$
$$-\frac{\left(\frac{m\pi}{a}\right)\left(\frac{n\pi}{b}\right)\left\{36ab\left(\frac{m\pi}{a}\right)\left(\frac{n\pi}{b}\right)\bar{R}_{1(c,p,s)}+24\ell\left[\bar{R}_{2(c,p,s)}+\bar{R}_{3(c,p,s)}\right]\right\}}{\left[\left(\frac{m\pi}{a}\right)^4 e^*_{22}+\left(\frac{m\pi}{a}\right)^2\left(\frac{n\pi}{b}\right)^2\left(2e^*_{12}+e^*_{66}\right)+\left(\frac{n\pi}{b}\right)^4 e^*_{11}\right]\left\{9a^2b^2\left(\frac{m\pi}{a}\right)^2\left(\frac{n\pi}{b}\right)^2-16\ell^2\right\}},$$

$$\bar{R}_{1(c)}=\pm\frac{2abH\left(\frac{m\pi}{a}\right)^2}{4H^2+b^2},\ \bar{R}_{2(c)}=\bar{R}_{3(c)}=\pm\frac{8H\left(\frac{m\pi}{a}\right)\ell}{3\left(\frac{n\pi}{b}\right)\left(4H^2+b^2\right)},$$

$$\bar{R}_{1(p,s)}=-\frac{1}{2}\left(\frac{m\pi}{a}\right)^2 a\int_0^b\frac{\sin^2\left(\frac{n\pi y}{b}\right)}{R_{(p,s)}}dy,\ \bar{R}_{2(p,s)}=-\frac{1}{3}\left(\frac{m\pi}{a}\right)\left[(-1)^m-1\right]\int_0^b\frac{\sin\left(\frac{n\pi y}{b}\right)}{R_{(p,s)}}dy,$$

$$\bar{R}_{3(p,s)} = \left(\frac{m\pi}{a}\right)\left[(-1)^m - 1\right]\int_0^b \frac{\sin\left(\frac{n\pi y}{b}\right)\cos\left(\frac{2n\pi y}{b}\right)}{R_{(p,s)}}dy.$$

Appendix B

$$\bar{y}_{11} = \frac{ab}{4}\left\{\begin{array}{l}\left[32e_{22}^{*}\bar{x}_{12}^{2} + e_{22}^{*}\bar{x}_{33}^{2} + \left(\frac{4}{3h^2}\right)^2 h_{11}^{*}\right]\left(\frac{m\pi}{a}\right)^4 + \left[l_{44}\left(\frac{12}{3h^2}\right)^2 - g_{44}\frac{8}{3h^2} + f_{44}\right]\left(\frac{m\pi}{a}\right)^2 \\ + \left[\left(h_{12}^{*} + h_{21}^{*} + 4h_{66}^{*}\right)\left(\frac{4}{3h^2}\right)^2 + \bar{x}_{33}^{2}\left(2e_{12}^{*} + e_{66}^{*}\right)\right]\left(\frac{m\pi}{a}\right)^2\left(\frac{n\pi}{b}\right)^2 \\ + \left[32e_{11}^{*}\bar{x}_{22}^{2} + e_{11}^{*}\bar{x}_{33}^{2} + \left(\frac{4}{3h^2}\right)^2 h_{22}^{*}\right]\left(\frac{n\pi}{b}\right)^4 + \left[l_{55}\left(\frac{12}{3h^2}\right)^2 - 6g_{55}\frac{4}{3h^2} + f_{55}\right]\left(\frac{n\pi}{b}\right)^2 \\ - \dfrac{32\left[\bar{x}_{12}e_{22}^{*}\left(\frac{m\pi}{a}\right)^4 + \left(\frac{m\pi}{a}\right)^2\left(\frac{n\pi}{b}\right)^2 e_{12}^{*}\left(\bar{x}_{12} + \bar{x}_{22}\right) + \left(\frac{n\pi}{b}\right)^4 \bar{x}_{22}e_{11}^{*}\right]\ell\bar{x}_{33}}{3ab\left(\frac{m\pi}{a}\right)\left(\frac{n\pi}{b}\right)}\end{array}\right\},$$

$$\bar{y}_{12} = \frac{ab}{8}\left\{\begin{array}{l}2\bar{x}_{31}\bar{x}_{33}\left(\frac{m\pi}{a}\right)^4 e_{22}^{*} + \left(\frac{n\pi}{b}\right)^2\left(4e_{12}^{*} + 2e_{66}^{*}\right)\bar{x}_{33}\bar{x}_{31}\left(\frac{m\pi}{a}\right)^2 + 2\bar{x}_{31}\bar{x}_{33}\left(\frac{n\pi}{b}\right)^4 e_{11}^{*} + \\ \left[\left(h_{12}^{*} + h_{21}^{*} + 4h_{66}^{*}\right)\left(\frac{n\pi}{b}\right)^2\left(\frac{4}{3h^2}\right)^2 - \left(\bar{c}_{21}^{*} + 2\bar{c}_{66}^{*} + c_{12}^{*} + 2c_{66}^{*}\right)\left(\frac{n\pi}{b}\right)^2\frac{4}{3h^2}\right]\left(\frac{m\pi}{a}\right) \\ + \left[18\left(\frac{4}{3h^2}\right)^2 l_{44} - 12g_{44}\frac{4}{3h^2} + 2f_{44}\right]\left(\frac{m\pi}{a}\right) + \frac{4}{3h^2}\left(\frac{8}{3h^2}h_{11}^{*} - c_{11}^{*} - \bar{c}_{11}^{*}\right)\left(\frac{m\pi}{a}\right)^3 \\ - \dfrac{32\left[\bar{x}_{12}e_{22}^{*}\left(\frac{m\pi}{a}\right)^4 + \left(\frac{m\pi}{a}\right)^2\left(\frac{n\pi}{b}\right)^2\left(\bar{x}_{12} + \bar{x}_{22}\right)e_{12}^{*} + \bar{x}_{22}\left(\frac{n\pi}{b}\right)^4 e_{12}^{*}\right]\bar{x}_{31}\ell}{3ab\left(\frac{m\pi}{a}\right)\left(\frac{n\pi}{b}\right)}\end{array}\right\},$$

$$\bar{y}_{13} = \frac{ab}{8}\left\{\begin{array}{l}2\bar{x}_{33}e_{11}^{*}\left(\frac{m\pi}{a}\right)\left(\frac{n\pi}{b}\right)^4\bar{x}_{32} + \frac{4}{3h^2}\left(\frac{8}{3h^2}h_{22}^{*} - c_{22}^{*} - \bar{c}_{22}^{*}\right)\left(\frac{n\pi}{b}\right)^3 + 2e_{22}^{*}\bar{x}_{33}\bar{x}_{32}\left(\frac{n\pi}{b}\right)^4 \\ \left[\left(h_{12}^{*} + h_{21}^{*} + 4h_{66}^{*}\right)\left(\frac{m\pi}{a}\right)^2\left(\frac{4}{3h^2}\right)^2 - \left(c_{21}^{*} + 2c_{66}^{*} + \bar{c}_{12}^{*} + 2\bar{c}_{66}^{*}\right)\left(\frac{m\pi}{a}\right)^2\frac{4}{3h^2}\right]\left(\frac{n\pi}{b}\right) \\ + \left[18\left(\frac{4}{3h^2}\right)^2 l_{55} - 12\frac{4}{3h^2}g_{55} + 2f_{55}\right]\left(\frac{n\pi}{b}\right) + \left(\frac{m\pi}{a}\right)^2\left(\frac{n\pi}{b}\right)^2\bar{x}_{32}\left(4e_{12}^{*} + 2e_{66}^{*}\right)\bar{x}_{33} \\ - \dfrac{32\left[\bar{x}_{12}\left(\frac{m\pi}{a}\right)^4 e_{22}^{*} + e_{12}^{*}\left(\frac{m\pi}{a}\right)^2\left(\frac{n\pi}{b}\right)^2\left(\bar{x}_{12} + \bar{x}_{22}\right) + \bar{x}_{22}\left(\frac{n\pi}{b}\right)^4 e_{11}^{*}\right]\ell\bar{x}_{32}}{3ab\left(\frac{m\pi}{a}\right)\left(\frac{n\pi}{b}\right)}\end{array}\right\},$$

$$\bar{y}_{14} = -8\left[\bar{x}_{11}e_{22}^{*}\left(\frac{m\pi}{a}\right)^4 + \left(\frac{m\pi}{a}\right)^2\left(\frac{n\pi}{b}\right)^2\left(\bar{x}_{11} + \bar{x}_{21}\right)e_{12}^{*} + \left(\frac{n\pi}{b}\right)^4\bar{x}_{21}e_{11}^{*}\right]\ell\bar{x}_{31}\Big/3\left(\frac{m\pi}{a}\right)\left(\frac{n\pi}{b}\right),$$

$$\bar{y}_{15}=-8\left[\bar{x}_{11}e_{22}^{*}\left(\frac{m\pi}{a}\right)^{4}+\left(\frac{m\pi}{a}\right)^{2}\left(\frac{n\pi}{b}\right)^{2}(\bar{x}_{11}+\bar{x}_{21})e_{12}^{*}+\left(\frac{n\pi}{b}\right)^{4}\bar{x}_{21}e_{11}^{*}\right]\ell\bar{x}_{32}\Big/3\left(\frac{m\pi}{a}\right)\left(\frac{n\pi}{b}\right),$$

$$\bar{y}_{17}=16ba\left[\bar{x}_{11}^{2}e_{22}^{*}\left(\frac{m\pi}{a}\right)^{4}+\bar{x}_{21}^{2}e_{11}^{*}\left(\frac{n\pi}{b}\right)^{4}\right],\ \bar{y}_{18}=\frac{4}{3h^{2}}\left[\left(\frac{m\pi}{a}\right)^{2}a_{11}^{*}+\left(\frac{n\pi}{b}\right)^{2}a_{12}^{*}\right]\ell\Big/\left(\frac{m\pi}{a}\right)\left(\frac{n\pi}{b}\right),$$

$$\bar{y}_{16}=-\frac{4\left[\bar{x}_{11}e_{22}^{*}\left(\frac{m\pi}{a}\right)^{4}+\left(\frac{m\pi}{a}\right)^{2}\left(\frac{n\pi}{b}\right)^{2}(\bar{x}_{11}+\bar{x}_{21})e_{12}^{*}+\left(\frac{n\pi}{b}\right)^{4}\bar{x}_{21}e_{11}^{*}\right]\ell\bar{x}_{33}}{\left(\frac{m\pi}{a}\right)\left(\frac{n\pi}{b}\right)}$$

$$+24ab\left[\bar{x}_{11}\bar{x}_{12}\left(\frac{m\pi}{a}\right)^{4}e_{22}^{*}+\bar{x}_{21}\bar{x}_{22}\left(\frac{n\pi}{b}\right)^{4}e_{11}^{*}\right],$$

$$\bar{y}_{19}=\left(\frac{m\pi}{a}\right)^{2}ab\Big/4,\ \bar{y}_{110}=\frac{-\bar{x}_{33}\left[\left(\frac{m\pi}{a}\right)^{2}e_{22}^{*}+\left(\frac{n\pi}{b}\right)^{2}e_{12}^{*}\right]\ell}{\left(\frac{m\pi}{a}\right)\left(\frac{n\pi}{b}\right)},\ \bar{y}_{112}=\frac{\ell}{\left(\frac{m\pi}{a}\right)\left(\frac{n\pi}{b}\right)},$$

$$\bar{y}_{113}=-\frac{\left[\left(a_{11}^{*}\Phi_{1x}^{*}+a_{21}^{*}\Phi_{1y}^{*}-\Phi_{4x}^{*}\right)\left(\frac{m\pi}{a}\right)^{2}+\left(\frac{n\pi}{b}\right)^{2}\left(a_{12}^{*}\Phi_{1x}^{*}+a_{22}^{*}\Phi_{1y}^{*}-\Phi_{4y}^{*}\right)\right]\frac{4}{3h^{2}}\ell}{\left(\frac{m\pi}{a}\right)\left(\frac{n\pi}{b}\right)},$$

$$\bar{y}_{22}=\frac{ab}{4}\left\{\begin{aligned}&\left[e_{22}^{*}\left(\frac{m\pi}{a}\right)^{4}+\left(\frac{n\pi}{b}\right)^{4}e_{11}^{*}+\left(\frac{m\pi}{a}\right)^{2}\left(\frac{n\pi}{b}\right)^{2}\left(2e_{12}^{*}+e_{66}^{*}\right)\right]\bar{x}_{31}^{2}\\&+\left[\left(\frac{4}{3h^{2}}\right)^{2}h_{11}^{*}+\left(-c_{11}^{*}-\bar{c}_{11}^{*}\right)\frac{4}{3h^{2}}+b_{11}^{*}\right]\left(\frac{m\pi}{a}\right)^{2}-6g_{44}\frac{4}{3h^{2}}\\&+\left[\left(\frac{4}{3h^{2}}\right)^{2}h_{66}^{*}+\left(-c_{66}^{*}-\bar{c}_{66}^{*}\right)\frac{4}{3h^{2}}+b_{66}^{*}\right]\left(\frac{n\pi}{b}\right)^{2}+9l_{44}\left(\frac{4}{3h^{2}}\right)^{2}+f_{44}\end{aligned}\right\},$$

$$\bar{y}_{115}=\frac{ab}{4}\int_{-h/2}^{h/2}\rho dz,\ \bar{y}_{116}=ab/4,$$

$$\bar{y}_{23}=\frac{ab}{4}\left\{\begin{aligned}&\left[e_{22}^{*}\left(\frac{m\pi}{a}\right)^{4}+\left(2e_{12}^{*}+e_{66}^{*}\right)\left(\frac{m\pi}{a}\right)^{2}\left(\frac{n\pi}{b}\right)^{2}+e_{11}^{*}\left(\frac{n\pi}{b}\right)^{4}\right]\bar{x}_{32}\bar{x}_{31}\\&+\frac{1}{2}\left(\frac{m\pi}{a}\right)\left(\frac{n\pi}{b}\right)\left[\begin{aligned}&\left(h_{12}^{*}+h_{21}^{*}+2h_{66}^{*}\right)\left(\frac{4}{3h^{2}}\right)^{2}+b_{21}^{*}+b_{12}^{*}+2b_{66}^{*}\\&+\left(-c_{12}^{*}-c_{21}^{*}-2c_{66}^{*}-\bar{c}_{12}^{*}-\bar{c}_{21}^{*}-2\bar{c}_{66}^{*}\right)\frac{4}{3h^{2}}\end{aligned}\right]\end{aligned}\right\},$$

$$\bar{y}_{24}=-\frac{4\left[\bar{x}_{11}e_{22}^{*}\left(\frac{m\pi}{a}\right)^{4}+\left(\frac{m\pi}{a}\right)^{2}\left(\frac{n\pi}{b}\right)^{2}(\bar{x}_{11}+\bar{x}_{21})e_{12}^{*}+\left(\frac{n\pi}{b}\right)^{4}\bar{x}_{21}e_{11}^{*}\right]\bar{x}_{31}\ell}{3\left(\frac{m\pi}{a}\right)\left(\frac{n\pi}{b}\right)},$$

$$\bar{y}_{25} = -\frac{\left(d_{11}^{*} - a_{11}^{*}\frac{4}{3h^2}\right)\ell}{\left(\frac{n\pi}{b}\right)}, \quad \bar{y}_{26} = -\frac{\left[\left(\frac{m\pi}{a}\right)^2 e_{22}^{*} + \left(\frac{n\pi}{b}\right)^2 e_{12}^{*}\right]\bar{x}_{31}\ell}{\left(\frac{m\pi}{a}\right)\left(\frac{n\pi}{b}\right)},$$

$$\bar{y}_{27} = \left[\left(-a_{11}^{*}\Phi_{1x}^{*} - a_{21}^{*}\Phi_{1y}^{*} + \Phi_{4x}^{*}\right)\frac{4}{3h^2} + d_{21}^{*}\Phi_{1y}^{*} + d_{11}^{*}\Phi_{1x}^{*} - \Phi_{2y}^{*}\right]\ell \Big/ \left(\frac{n\pi}{b}\right),$$

$$\bar{y}_{33} = \frac{ab}{4}\left\{\begin{aligned}&\left[e_{22}^{*}\left(\frac{m\pi}{a}\right)^4 + \left(\frac{n\pi}{b}\right)^4 e_{11}^{*} + \left(\frac{m\pi}{a}\right)^2\left(\frac{n\pi}{b}\right)^2\left(2e_{12}^{*} + e_{66}^{*}\right)\right]\bar{x}_{32}^2 \\ &+\left[\left(\frac{4}{3h^2}\right)^2 h_{22}^{*} + \left(-c_{22}^{*} - \bar{c}_{22}^{*}\right)\frac{4}{3h^2} + b_{22}^{*}\right]\left(\frac{n\pi}{b}\right)^2 - 6e_{55}\frac{4}{3h^2} \\ &+\left[\left(\frac{4}{3h^2}\right)^2 h_{66}^{*} + \left(-c_{66}^{*} - \bar{c}_{66}^{*}\right)\frac{4}{3h^2} + b_{66}^{*}\right]\left(\frac{m\pi}{a}\right)^2 + 9l_{55}\left(\frac{4}{3h^2}\right)^2 + f_{55}\end{aligned}\right\},$$

$$\bar{y}_{34} = -4\left[\bar{x}_{11}e_{22}^{*}\left(\frac{m\pi}{a}\right)^4 + \left(\frac{m\pi}{a}\right)^2\left(\frac{n\pi}{b}\right)^2\left(\bar{x}_{11} + \bar{x}_{21}\right)e_{12}^{*} + \left(\frac{n\pi}{b}\right)^4 \bar{x}_{21}e_{11}^{*}\right]\bar{x}_{32}\ell \Big/ 3\left(\frac{m\pi}{a}\right)\left(\frac{n\pi}{b}\right),$$

$$\bar{y}_{35} = \frac{\left(a_{12}^{*}\frac{4}{3h^2} - d_{12}^{*}\right)\ell}{\left(\frac{m\pi}{a}\right)}, \quad \bar{y}_{36} = -\frac{\bar{x}_{32}\left[\left(\frac{m\pi}{a}\right)^2 e_{22}^{*} + \left(\frac{n\pi}{b}\right)^2 e_{12}^{*}\right]\ell}{\left(\frac{m\pi}{a}\right)\left(\frac{n\pi}{b}\right)},$$

$$\bar{y}_{37} = \left[\left(-a_{12}^{*}\Phi_{1x}^{*} - a_{22}^{*}\Phi_{1y}^{*} + \Phi_{4y}^{*}\right)\frac{4}{3h^2} + d_{22}^{*}\Phi_{1y}^{*} + d_{12}^{*}\Phi_{1x}^{*} - \Phi_{2y}^{*}\right]\ell \Big/ \left(\frac{m\pi}{a}\right),$$

$$b_{11}^{*} = -d_{11}d_{11}^{*} - d_{12}d_{21}^{*} + b_{11}, \quad b_{12}^{*} = -d_{11}d_{12}^{*} - d_{12}d_{22}^{*} + b_{12},$$
$$b_{66}^{*} = -d_{66}d_{66}^{*} + b_{66}, \quad b_{21}^{*} = -d_{12}d_{11}^{*} - d_{22}d_{21}^{*} + b_{12}, \quad b_{22}^{*} = -d_{12}d_{12}^{*} - d_{22}d_{22}^{*} + b_{22},$$

$$c_{11}^{*} = -d_{11}a_{11}^{*} - d_{12}a_{21}^{*} + c_{11}, \quad c_{12}^{*} = -d_{11}a_{12}^{*} - d_{12}a_{22}^{*} + c_{12},$$
$$c_{66}^{*} = -d_{66}a_{66}^{*} + c_{66}, \quad c_{21}^{*} = -d_{12}a_{11}^{*} - d_{22}a_{21}^{*} + c_{12}, \quad c_{22}^{*} = -d_{12}a_{12}^{*} - d_{22}a_{22}^{*} + c_{22},$$

$$\bar{c}_{11}^{*} = -a_{11}d_{11}^{*} - a_{12}d_{21}^{*} + c_{11}, \quad \bar{c}_{12}^{*} = -a_{11}d_{12}^{*} - a_{12}d_{22}^{*} + c_{12},$$
$$\bar{c}_{66}^{*} = -a_{66}d_{66}^{*} + c_{66}, \quad \bar{c}_{21}^{*} = -a_{12}d_{11}^{*} - a_{22}d_{21}^{*} + c_{12}, \quad \bar{c}_{22}^{*} = -a_{12}d_{12}^{*} - a_{22}d_{22}^{*} + c_{22},$$

$$h_{11}^{*} = -a_{11}a_{11}^{*} - a_{12}a_{21}^{*} + h_{11}, \quad h_{12}^{*} = -a_{11}a_{12}^{*} - a_{12}a_{22}^{*} + h_{12},$$
$$h_{66}^{*} = -a_{66}a_{66}^{*} + h_{66}, \quad h_{21}^{*} = -a_{12}a_{11}^{*} - a_{22}a_{21}^{*} + h_{12}, \quad h_{22}^{*} = -a_{12}a_{12}^{*} - a_{22}a_{22}^{*} + h_{22}.$$

$$\bar{y}_{41} = -\left[\left(\frac{m\pi}{a}\right)^2\left(\bar{x}_{33}e_{12}^{*} - \frac{4}{3h^2}a_{11}^{*}\right) - \left(\frac{n\pi}{b}\right)^2\left(\frac{4}{3h^2}a_{12}^{*} - \bar{x}_{33}e_{11}^{*}\right)\right]\ell \Big/ \left(\frac{m\pi}{a}\right)\left(\frac{n\pi}{b}\right),$$

$$\bar{y}_{42} = \left[\bar{x}_{31}\left(\frac{m\pi}{a}\right)^2 e_{12}^{*} + \left(d_{11}^{*} - \frac{4}{3h^2}a_{11}^{*}\right)\left(\frac{m\pi}{a}\right) + \left(\frac{n\pi}{b}\right)^2 \bar{x}_{31}e_{11}^{*}\right]\ell \Big/ \left(\frac{m\pi}{a}\right)\left(\frac{n\pi}{b}\right),$$

$$\bar{y}_{43} = \left[\bar{x}_{32}\left(\frac{n\pi}{b}\right)^2 e_{11}^{*} + \left(d_{12}^{*} - \frac{4}{3h^2}a_{12}^{*}\right)\left(\frac{n\pi}{b}\right) + \bar{x}_{32}\left(\frac{m\pi}{a}\right)^2 e_{12}^{*}\right]\ell \Big/ \left(\frac{m\pi}{a}\right)\left(\frac{n\pi}{b}\right),$$

$$\bar{y}_{44} = \frac{-ab\left(\frac{m\pi}{a}\right)^2}{8},\ \bar{y}_{45} = e^*_{11}ab,\quad \bar{y}_{46} = e^*_{12}ab,\quad \bar{y}_{47} = \left(e^*_{11}\Phi^*_{1x} + e^*_{12}\Phi^*_{1y}\right)ab,$$

$$\bar{y}_{51} = \left[\left(\frac{m\pi}{a}\right)^2\left(\frac{4}{3h^2}a^*_{21} - \bar{x}_{33}e^*_{22}\right) + \left(\frac{n\pi}{b}\right)^2\left(\frac{4}{3h^2}a^*_{22} - \bar{x}_{33}e^*_{12}\right)\right]\ell \Big/ \left(\frac{m\pi}{a}\right)\left(\frac{n\pi}{b}\right) + \bar{R}_{4(c,p,s)},$$

$$\bar{y}_{52} = -\left[\left(\frac{m\pi}{a}\right)^2 \bar{x}_{31}e^*_{22} + \left(\frac{4}{3h^2}a^*_{21} - d^*_{21}\right)\left(\frac{m\pi}{a}\right) + \left(\frac{n\pi}{b}\right)^2 \bar{x}_{31}e^*_{12}\right]\ell \Big/ \left(\frac{m\pi}{a}\right)\left(\frac{n\pi}{b}\right),$$

$$\bar{y}_{53} = -\left[\bar{x}_{32}\left(\frac{n\pi}{b}\right)^2 e^*_{12} + \left(\frac{4}{3h^2}a^*_{22} - d^*_{22}\right)\left(\frac{n\pi}{b}\right) + \bar{x}_{32}\left(\frac{m\pi}{a}\right)^2 e^*_{22}\right]\ell \Big/ \left(\frac{m\pi}{a}\right)\left(\frac{n\pi}{b}\right),$$